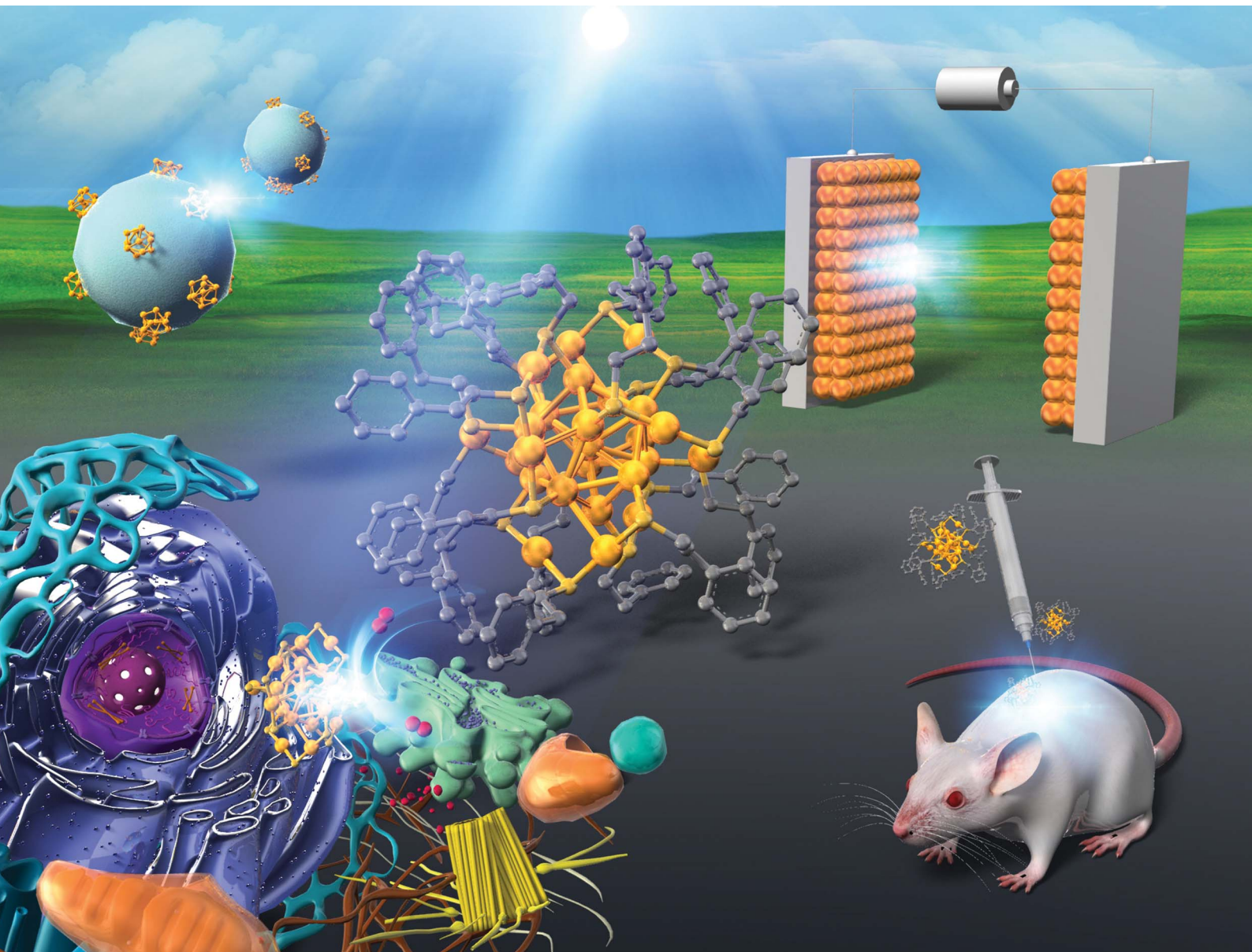
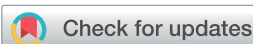


# Nanoscale Advances

[rsc.li/nanoscale-advances](http://rsc.li/nanoscale-advances)



ISSN 2516-0230



Cite this: *Nanoscale Adv.*, 2020, **2**, 17

Received 15th September 2019  
Accepted 17th October 2019

DOI: 10.1039/c9na00583h  
[rsc.li/nanoscale-advances](http://rsc.li/nanoscale-advances)

## Photo/electrocatalysis and photosensitization using metal nanoclusters for green energy and medical applications

Tokuhisa Kawawaki,  <sup>a</sup> Yuichi Negishi,  <sup>\*a</sup> and Hideya Kawasaki  <sup>\*b</sup>

Owing to the rapidly increasing demand for sustainable technologies in fields such as energy, environmental science, and medicine, nanomaterial-based photo/electrocatalysis has received increasing attention. Recently, synthetic innovations have allowed the fabrication of atomically precise metal nanoclusters (NCs). These NCs show potential for green energy and medical applications. The present article primarily focuses on evaluation of the recent developments in the photo/electrocatalytic and photosensitizing characteristics of metal and alloy NCs. The review comprises two sections: (i) photo/electrocatalysis for green energy and (ii) photosensitization for biomedical therapy applications. Finally, the challenges associated with the use of metal NCs are presented on the basis of current developments.

## 1. Introduction

During the past few decades, photocatalysis and electrocatalysis have received significant attention as a result of the increasing demand for sustainable technologies in the fields of energy, environmental science, and medicine.<sup>1–7</sup> Photo/electrocatalytic approaches rely on electronic excitation, and their performance depends on the ability to create electron ( $e^-$ )-hole ( $h^+$ ) pairs that successively undergo chemical reactions with other

compounds *via* oxidative (*e.g.*,  $2H_2O(l) \rightarrow O_2(g) + 4H^+(aq) + 4e^-$ ) and reductive reactions (*e.g.*,  $2H^+(aq) + 2e^- \rightarrow H_2(g)$ ). Many advanced nanomaterial-based photo/electrocatalysts have been synthesized and reported, and their advantages include large surface-to-volume effects, numerous catalytic active sites, quantum size effects and high stability.<sup>1–7</sup> These catalysts are considered to be promising for energy and environmental applications, such as photo/electro water splitting to generate hydrogen ( $H_2$ ) and conversion of carbon dioxide ( $CO_2$ ). Furthermore, they are used in the fuel industry and in water treatment and disinfection, air purification, and self-cleaning surfaces.<sup>1–6</sup> Usually, the term “photo/electrocatalysis” refers to photo/electrochemical reactions, which involve an electron transfer. Conversely, when energy transfer occurs in

<sup>a</sup>Department of Applied Chemistry, Faculty of Science, Tokyo University of Science, 1-3 Kagurazaka, Shinjuku-ku, Tokyo 162-8601, Japan. E-mail: negishi@rs.kagu.tus.ac.jp

<sup>b</sup>Department of Chemistry and Materials Engineering, Faculty of Chemistry, Materials and Bioengineering, Kansai University, Suita-shi, Osaka 564-8680, Japan. E-mail: hkawa@kansai-u.ac.jp



Assistant Professor of the Department of Applied Chemistry, Faculty of Science, Tokyo University of Science, received PhD degree (2015) in Applied Chemistry from the University of Tokyo. Since 2016, he worked as Japan Society for the Promotion of Science (JSPS) Postdoctoral fellow (PD) at the University of Melbourne. Since 2017, he worked as JSPS super PD (SPD) at Kyoto University. In 2019, he moved to the current position. His current research topics include synthesis of metal nanoparticles and nanoclusters in solutions and their applications for photoelectrochemistry.



Professor of the Department of Applied Chemistry at Tokyo University of Science. He received his PhD degree in Chemistry in 2001 under the supervision of Prof. Atsushi Nakajima from Keio University. Before joining Tokyo University of Science in 2008, he was employed as an assistant professor at Keio University and at the Institute for Molecular Science. His current research interests include the precise synthesis of stable and functionalised metal nanoclusters and their applications in energy and environmental materials.

a photochemical reaction, the process is often called “photosensitization”. Triplet photosensitizers are used not only for triplet energy transfer, but are also utilized in photodynamic therapy (PDT) for medical applications.<sup>7</sup>

One drawback of these nanomaterial-based photo/electrocatalysts is that they are generally poly-dispersed in size, morphology, and chemical composition. The heterogeneity of photo/electrocatalysts with multiple active sites often results in different catalytic activities and varying catalytic selectivity. Therefore, it is important to fabricate nanomaterial-based photo/electrocatalysts that can be controlled well at the atomic level.

Recent synthetic innovations have allowed the fabrication of atomically precise metal nanoclusters (NCs).<sup>8–18</sup> These metal NCs contain a few to hundreds of metal atoms that are protected by organic ligands (*e.g.*, thiolate, phosphine, small molecules, synthetic polymers, and biomolecules). Particularly, thiolate-protected metal NCs and their alloy NCs can be prepared with atomic precision as  $M_n(SR)_m$  ( $M$  = gold (Au), silver (Ag), copper (Cu), platinum (Pt), palladium (Pd), or other element; SR = thiolate ligand) in a wide range of sizes by varying the  $n$  and  $m$  values. As mentioned previously, such NCs have potential applications in the fields of energy, environmental science, medicine, and other.<sup>9–13</sup> The  $M_n(SR)_m$  NCs have discrete energy levels due to the quantum size effect, making them significantly different from the larger ( $>3$  nm) plasmonic metal (Au or Ag) nanoparticles (NPs) with continuous energy levels. By adjusting  $n$  and  $m$ , one can control the discrete electronic/geometrical structure of  $M_n(SR)_m$  NCs and thereby their photosensitizing and photo/electrocatalytic capability. Recently, several excellent reviews have discussed the syntheses of metal NCs,<sup>13</sup> photoluminescence,<sup>14</sup> and their biomedical<sup>15–17</sup> and catalytic applications.<sup>18</sup> However, to the best of our knowledge, there are no publications focusing on the photo/electrocatalytic and photosensitizing characteristics of metal NCs for applications in the green energy and medical fields. Therefore, a survey of recent progress, with a view to improving the photo/electrocatalytic and photosensitizing capability of metal NCs is needed.



Professor of the Department of Chemistry and Materials Engineering, Kansai University, received Doctor degree (1996) in science from Kyushu University. Since 1999, he worked as an assistant professor at Kyushu University. In 2006, he moved to be an Associate Professor at the Department of Chemistry and Materials Engineering, Kansai University. His current research interests include synthesis of photo-functionalised metal nanoclusters and their applications for catalysis, sensing, and biomedical fields.

photo-functionalised metal nanoclusters and their applications for catalysis, sensing, and biomedical fields.

In this review, we discuss recent achievements and evaluate the photo/electrocatalytic and photosensitizing characteristics of metal NCs and their alloy NCs. The review comprises two sections: (i) photo/electrocatalysis and photosensitization for green energy applications (specifically solar cell), and (ii) photosensitization for medical therapeutic applications (Fig. 1). We hope to provide a clear picture on how the photo/electrocatalytic and photosensitizing capability of metal NCs can improve their performance and promote the development of new green energy and medical applications.

## 2. Photo/electrocatalysis of metal NCs for green energy applications

In this section, we discuss recent progress of the photo/electrocatalytic (specifically reaction of water splitting and fuel cells) and photosensitizing applications (specifically solar cell) of metal NCs (Pd, Ag, Pt, or Au) and their alloy NCs. We summarized references used in this section in Table 1.

### 2.1. Electrocatalytic applications for water splitting

Water electrolysis is one of the cleanest energy-producing processes, generating  $H_2$  using only water and electricity, which is regarded as the next-generation energy source or raw material for chemicals. Water electrolysis comprises two half-reactions, which are the  $H_2$  evolution reaction (HER) and the  $O_2$  evolution reaction (OER). When supplying electricity to metal electrodes, a reduction reaction occurs on the cathode and an oxidation reaction on the anode, and thereby water molecules are split into  $H_2$  and  $O_2$ . However, the reaction does not proceed if the voltage supplied to the electrodes is higher than the redox potential of each reaction (HER: 0 V *vs.* SHE, OER: 1.23 V *vs.* SHE) due to the high activation energy. Therefore, investigations have been conducted to enhance the reactions using metal catalysts, such as precious metal NPs. An increased specific surface area of the active sites in the metal

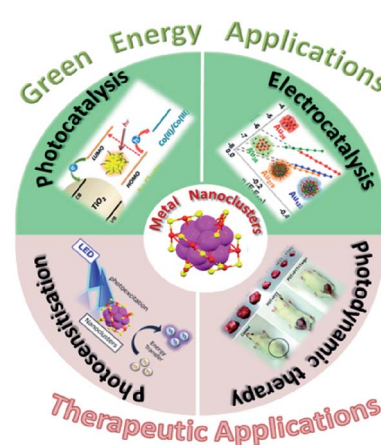


Fig. 1 Schematic of photo/electrocatalysis and photosensitization using metal NCs for green energy and medical applications. Reprinted with permission from ref. 51 and 75. Copyright American Chemical Society; ref. 127, Copyright 2015 Royal Society of Chemistry.



**Table 1** Chemical reaction and summarized references in Section 2

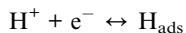
Section	Reaction	Clusters	References
2.1.1	H <sub>2</sub> evolution reaction	Pt	24 and 25
2.1.1	H <sub>2</sub> evolution reaction	Pd	26 and 34
2.1.1	H <sub>2</sub> evolution reaction	Au	27–34
2.1.2	O <sub>2</sub> evolution reaction	Pd	26
2.1.2	O <sub>2</sub> evolution reaction	Au	40 and 41
2.2	Electrocatalytic reaction for fuel cells	Pt	45–48 and 55
2.2	Electrocatalytic reaction for fuel cells	Au	49–54 and 56
2.3	Photocatalytic water splitting reaction	Pt	58 and 59
2.3	Photocatalytic water splitting reaction	Au	60–64, 67 and 68
2.3	Photocatalytic water splitting reaction	Ag	65 and 66
2.4	Redox reaction for solar cell	Au	69, 71 and 73–78
2.4	Redox reaction for solar cell	Ag	70 and 72–74
2.4	Redox reaction for solar cell	Pt	71
2.4	Redox reaction for solar cell	Pd	71

catalysts significantly increases the reaction rate per unit area. Hence, research on the improvement of the synthetic techniques to obtain fine metal particles has progressed. According to the Sabatier principle of chemical reactions occurring on the surface of a catalyst, the maximum activity is attained when the free energy of the adsorption and desorption of the reagents on the metal catalyst is the lowest. Consequently, the activity is closely related to the energy level (Fermi level) of the d-band center of each metal and the geometrical structure of the surface, which depends on the crystal plane and interatomic distances. These characteristics result in the tendency to form peaks in the activity volcano plots. The optimum metal types and their alloy NPs have been prepared based on the activity volcano plots obtained using various metal elements. Further reduction of the metal particle sizes induces the appearance of novel electronic and/or geometrical structures, which are different from the bulk metal. Therefore, recently, a number of studies on the electrocatalytic application of metal NCs composed of approximately several tens of atoms or less have been reported.

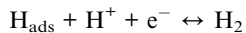
**2.1.1. H<sub>2</sub> evolution reaction.** HER, the half-reaction of water splitting, proceeds through the Volmer–Heyrovsky or Volmer–Tafel mechanism, whereby metal surface atoms form bonding orbitals with protons, resulting in the production of H<sub>2</sub>.

Under acidic conditions, the reaction proceeds as follows:

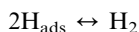
Volmer reaction:



Heyrovsky reaction:

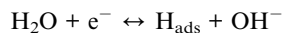


Tafel reaction:

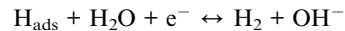


On the other hand, under alkaline conditions, the following reaction sequence occurs:

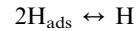
Volmer reaction:



Heyrovsky reaction:



Tafel reaction:



Here, the “ads” subscript denotes a reaction site on the catalyst surface. So far, noble metals, such as Pt, have been known for their high activity in HER, and attempts have been made to increase this activity further *via* miniaturization of the metals, and to predict their activity using density functional theory (DFT) calculations.<sup>19–23</sup> For example, Sun *et al.* studied the HER characteristics by preparing single Pt atoms and Pt NCs supported on nitrogen-doped graphene nanosheets (NGNs) using the atomic layer deposition technique. The results revealed that the HER activity of Pt atoms on Pt NCs (ALD50Pt) was 10.1 A mg<sup>-1</sup>, which is 37.4 times higher than the activity of the commercial carbon-supported Pt NP (Pt/C) catalyst (0.27 A mg<sup>-1</sup>) (Fig. 2A and B).<sup>24</sup> Furthermore, Chen *et al.* demonstrated that Pt NCs confined in a calixarene-based Ni<sub>24</sub> coordination cage (Fig. 2C) show much higher activity in HER than the commercial Pt/C catalyst (Fig. 2D and E).<sup>25</sup> The same group also reported that the activated carbon-supported Pd<sub>6</sub> (Pd<sub>6</sub>/AC-V; the ligands were removed in this case) shows the current density 10.22 times higher than the commercial Pt/C catalyst at –0.423 V.<sup>26</sup>

In contrast, bulk Au, which belongs to group 11, shows almost no HER activity. Reduction of the size to the cluster region, however, results in changes in the electronic structure, and thereby Au NCs exhibit HER activity. Based on the recent studies, Au NCs can now be synthesized using a very simple and easy approach. Moreover, the sizes can be controlled at atomic precision and their functions can be modulated *via* ligand exchange and heteroatom doping. In recent years, a number of studies have been conducted on the HER activity of Au NCs. For example, Teranishi and Sakamoto *et al.* studied the effect of the ligand structure on the HER activity using porphyrin-coordinated Au NCs (Fig. 3).<sup>27</sup> In their study, the distance between the porphyrin-ring and the surface sulfur (S) directly bonded to Au NCs was controlled by varying the number of methylene groups between those moieties (Fig. 3A and C). They found that the HER activity increases with decreasing distance between the porphyrin-ring and the Au NC surface (Fig. 3G and H). In addition, it was demonstrated that tetrakis-5 $\alpha$ ,10 $\alpha$ ,15 $\alpha$ ,20 $\alpha$ -(2-acetylthiomethylphenyl) porphyrin (SC<sub>1</sub>P)-protected Au NCs, with a 3.4 Å distance between the porphyrin-ring and the Au NC surface, show a high current density of 460% at 0.4 V *vs.* RHE, in comparison with Au NCs protected by ordinary phenylethanethiolate (PET). The study also demonstrates that the ligand structure strongly affects the HER activity and that the smaller Au<sub>n</sub>(SR)<sub>m</sub> NCs exhibit the higher HER activity.



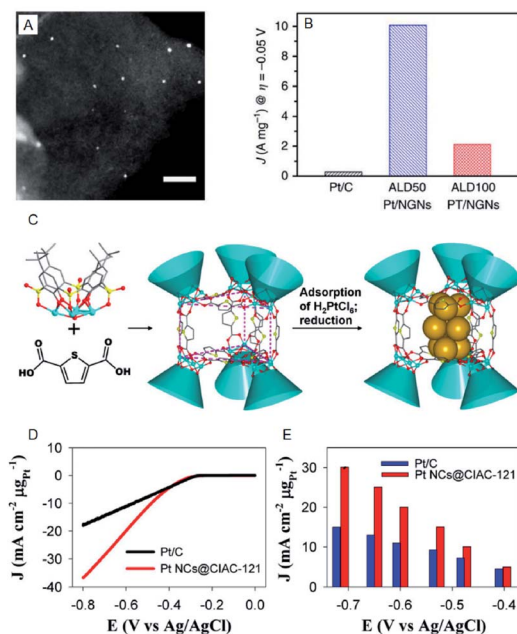


Fig. 2 (A) The annular dark-field scanning transmission electron microscopy (SEM) image of ALD50Pt/nitrogen-doped graphene nanosheets (NGNs). Scale bar shows the length of 20 nm. (B) HER current density of Pt/C, ALD50Pt/NGNs and ALD100Pt/NGNs. (C) Illustration of the assembly of trigonal prismatic  $\{\text{Ni}_{24}\}$  coordination cage (CIAC-121) and the fabrication of ultrafine Pt NCs. (D) The HER polarization curves. (E) Mass HER activity of Pt NCs@CIAC trigonal prismatic coordination cage ( $\{\text{Ni}_{24}(\text{TC4A-SO}_2)_6(\text{TDC})_{12}(\text{H}_2\text{O})_6\}$ ,  $\text{H}_4\text{TC4A-SO}_2 = p$ -tert-butylsulfonylcycl[4]arene;  $\text{H}_2\text{TDC} = 2,5$ -thiophenedicarboxylic acid). Panels (a) and (b) are reproduced with permission from ref. 24. Copyright 2016 Springer Nature. Panels (c), (d) and (e) are reproduced with permission from ref. 25. Copyright 2016 American Chemical Society.

On the other hand, Lee and Jiang *et al.* investigated the effect of heteroatom doping of  $\text{Au}_n(\text{SR})_m$  NCs on the HER activity.<sup>28-31</sup> They examined the HER activity of hexanethiolate (C6)-protected  $\text{Au}_{25}$  and  $\text{PtAu}_{24}$  NCs in a tetrahydrofuran (THF) electrolyte containing 1.0 M trifluoroacetic acid (TFA) (Fig. 4A–C). The obtained results demonstrated that  $\text{PtAu}_{24}$  NC has better catalytic activity with a higher starting potential ( $-0.89 \text{ V}$ ) than  $\text{Au}_{25}$  NC ( $-1.10 \text{ V}$ ). The same research group showed that the improved catalyst current and turnover frequency can be obtained even with Pd as the central atom, instead of Pt ( $\text{PtAu}_{24} > \text{PdAu}_{24} > \text{Au}_{25}$ ). The same tendency can be observed for the other-sized C6-protected  $\text{Au}_{38}$  NCs ( $\text{PtAu}_{36} > \text{PdAu}_{36} > \text{Au}_{38}$ ).<sup>32</sup> These results are in good agreement with those obtained from DFT calculations, which predicted that the HER activity significantly varies depending on the doping elements. Hence, the control of the electronic structure by alloying at the atomic level greatly affects the HER activity in the cluster size range.

In addition to these studies, Jin *et al.* investigated the HER activity of the composite comprising PET-protected  $\text{Au}_{25}$  NCs and molybdenum disulfide ( $\text{MoS}_2$ ) nanosheet ( $\text{MoS}_2$  nanosheet carrying PET-protected  $\text{Au}_{25}$ ;  $\text{Au}_{25}/\text{MoS}_2$ ; Fig. 4D and E).<sup>33</sup> The  $\text{Au}_{25}/\text{MoS}_2$  showed a current density 1.79 times higher than that of  $\text{MoS}_2$  at  $-0.4 \text{ V}$ , indicating that the improvement of HER

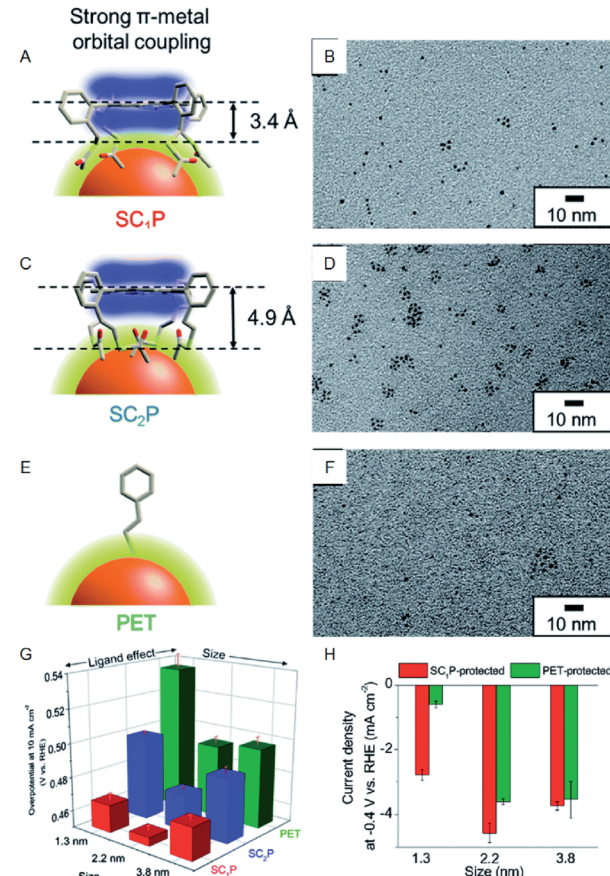


Fig. 3 (A), (C), and (E) Schematic of coordination fashions of  $\text{SC}_1\text{P}$ . (A) Tetrakis-5 $\alpha$ ,10 $\alpha$ ,15 $\alpha$ ,20 $\alpha$ -(2-acetylthioethylphenyl) porphyrin ( $\text{SC}_2\text{P}$ ; A) and PET (E) at the surface of Au NCs. (B), (D), and (F) TEM images of 1.3, 2.2, and 3.8 nm Au NCs protected with  $\text{SC}_1\text{P}$ , respectively. (G) Comparison of overpotential at  $-10 \text{ mA cm}^{-2}$ . (H) Current density at  $-0.4 \text{ V}$  of each size of Au NCs protected with each ligand. Panels (a)–(h) are reproduced with permission from ref. 27. Copyright 2018 Royal Society of Chemistry.

activity of  $\text{MoS}_2$  nanosheet was caused by loading  $\text{Au}_{25}$  NCs. X-ray photoelectron spectroscopy analysis showed that a negative shift of  $\sim 0.4 \text{ eV}$  in the Mo 3d orbital energy was induced by loading  $\text{Au}_{25}$  NCs. This implies that the partial charge transfer occurs from  $\text{Au}_{25}$  NCs to  $\text{MoS}_2$ , leading to the increased HER activity. The HER activity of the composite is, therefore, considerably improved by the electronic interaction between the materials. Regarding the HER activity of the composite comprising  $\text{MoS}_2$ , Zhu *et al.* also evaluated  $\text{Au}_2\text{Pd}_6/\text{MoS}_2$ .<sup>34</sup>

### 2.1.2. $\text{O}_2$ evolution reaction.

OER is a multi-step four-electron reaction dependent on the binding energy of the OER intermediate ( $\text{O}_2, \text{OH}, \text{OOH}$ , etc.).

Under acidic conditions, the reaction proceeds as follows:



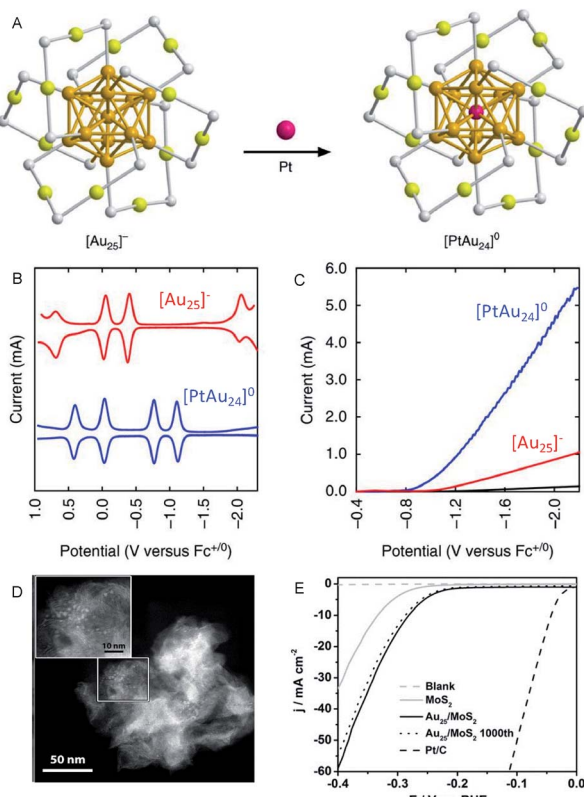
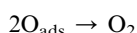
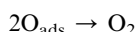
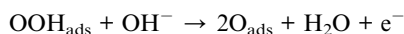
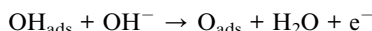


Fig. 4 (A) Geometrical structures of C6-protected  $\text{Au}_{25}$  and  $\text{PtAu}_{24}$  NCs (golden, gold atoms of the core; olive, gold atoms of the shell; grey, sulfur). (B) The square-wave voltammogram. (C) HER polarization curves of C6-protected  $\text{Au}_{25}$  and  $\text{PtAu}_{24}$  NCs. (D) High angle annular dark-field SEM (HAADF-STEM) images. Panels (a)–(c) are reproduced with permission from ref. 29. Copyright 2017 Springer Nature. Panels (d) and (e) are reproduced with permission from ref. 33. Copyright 2017 Wiley-VCH.



On the other hand, under alkaline conditions, the following reaction sequence takes place:



According to this reaction pathway, the OER activity of the catalyst generally depends on the binding energy of the OER intermediates on the surface (O, OH, OOH, etc.). An appropriate binding energy of the oxygen species (neither too high nor too low) enables the catalyst suitable for OER. For this reason, the

metal oxides, such as iridium oxide ( $\text{IrO}_x$ ), ruthenium oxide ( $\text{RuO}_x$ ), exhibit high activity. Therefore, extensive efforts have been made on their miniaturization, the theoretical prediction of the activity and the mechanism.<sup>35–38</sup>

Moreover, research regarding cluster-sized particles is progressing. Chen and Gao reported that dodecanethiolate (C12)-protected  $\text{Pd}_6/\text{AC}$  exhibits a current density 37 times higher than that of commercially available Pt/C at an applied voltage of 1.85 V (Fig. 5A and B).<sup>26</sup> Although ligands were considered to be disadvantageous for electrode reactions, this study revealed that the higher electron density of C12-protected  $\text{Pd}_6/\text{AC}$  enhances the desorption process of oxygen atoms or molecules and is favorable for OER. In addition, there are several reports describing the suitability of  $\text{M}_n(\text{SR})_m$  NCs for OER. For example, Hussain and Joya *et al.* reported that the OER activity of  $\text{Ni}_4(\text{PET})_8$  NC is equal to that of a  $\text{RuO}_2$  electrocatalyst.<sup>39</sup>

As with HER activity, OER activity has also been studied for the composites including Au NCs. Jin *et al.* investigated the OER activity of the composite comprising PET-protected  $\text{Au}_{25}$  NCs and cobalt diselenide ( $\text{CoSe}_2$ ) nanosheet ( $\text{CoSe}_2$  nanosheet carrying PET-protected  $\text{Au}_{25}$ ;  $\text{Au}_{25}/\text{CoSe}_2$ ) and revealed that  $\text{Au}_{25}/\text{CoSe}_2$  shows a current density of  $10 \text{ mA cm}^{-2}$  with a small overvoltage of approximately 0.43 V ( $\sim 0.52 \text{ V}$  with  $\text{CoSe}_2$  alone) (Fig. 6).<sup>40</sup> The group also investigated the effect of Au NC size on OER activity using a series of  $\text{Au}_n(\text{SR})_m$  NCs ( $\text{Au}_{10}$ ,  $\text{Au}_{25}$ ,  $\text{Au}_{144}$ , and  $\text{Au}_{333}$ ). It was revealed that OER activity increases with increasing the Au NC size. Furthermore, Peng and Zeng demonstrated that Au NC/ $\text{CoSe}_2$  is superior for increasing the OER activity compared to commercially available Ir/C.<sup>41</sup>

## 2.2. Electrocatalytic application for fuel cells

The ultimate energy-conversion systems used for power generation are fuel cells utilizing materials such as  $\text{H}_2$  and methanol obtained from natural energy sources. Such methods involve circulating energy systems that do not use any fossil fuels and only release water as the waste product.

Fuel cells are roughly classified into those using alcohol and those using  $\text{H}_2$ . The latter involves the  $\text{H}_2$  oxidation reaction (HOR) and  $\text{O}_2$  reduction reaction (ORR), which are the reverse reactions of HER and OER, respectively. HOR is a one-electron reaction system where the catalysts displaying HER-activity can be useful. In contrast, ORR is a four-electron reaction system, and since it proceeds through a complex reaction pathway, its reactivity is different from that of OER.

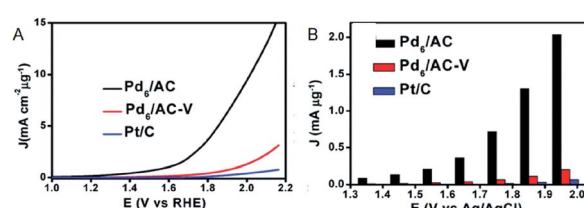


Fig. 5 (A) OER polarization curves. (B) Mass OER activity of  $\text{Pd}_6/\text{AC}$ ,  $\text{Pd}_6/\text{AC-V}$  and Pt/C at each overpotential. Panels (a) and (b) are reproduced with permission from ref. 26. Copyright 2017 Royal Society of Chemistry.



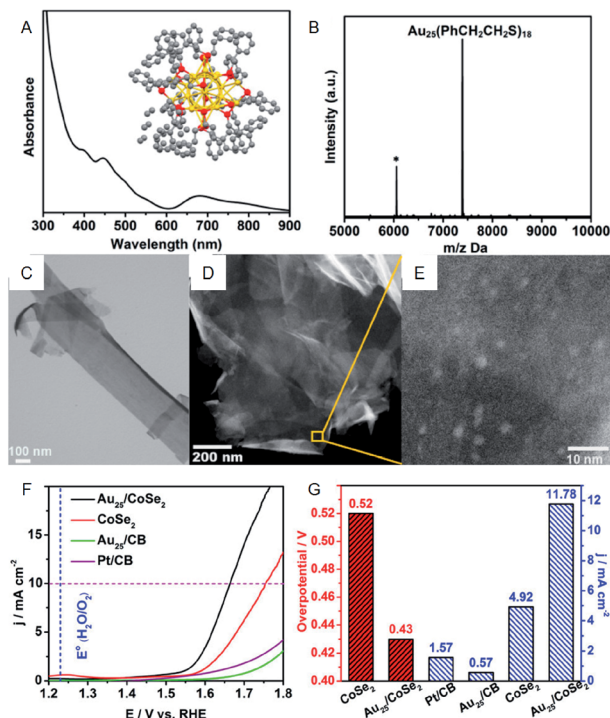
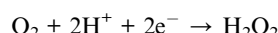
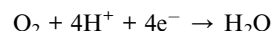
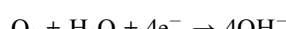


Fig. 6 (A) UV-vis and (B) MALDI-mass characterization of Au<sub>25</sub>(PET)<sub>18</sub> NCs. Inset of (A): crystal structure of Au<sub>25</sub>(PET)<sub>18</sub> NCs. (C) TEM image of CoSe<sub>2</sub> nanosheets. (D) and (E) HAADF-STEM images of Au<sub>25</sub>/CoSe<sub>2</sub> composite with different magnifications. (F) OER polarization curves. (G) Mass OER activity of Au<sub>25</sub>/CoSe<sub>2</sub> composite, CoSe<sub>2</sub>, Au<sub>25</sub> supported on carbon black (CB) and commercial Pt/CB. Panels (a)–(g) are reproduced with permission from ref. 40. Copyright 2017 American Chemical Society.

Under acidic conditions, ORR proceeds as follows:



On the other hand, under alkaline conditions, the following reaction sequence takes place:



The first step in both of these reaction pathways is the scission of the O–O bond. Regarding fuel cell applications, the theoretical redox potential of the direct four-electron pathway is 1.23 V vs. SHE, which is greater than that of the indirect two-electron pathway (0.68 V vs. SHE). Therefore, the direct four-electron pathway is the preferred reaction system, owing to the higher energy-conversion efficiency. Since the ORR on the

reduction side is slower than on the oxidation side, the former is the rate-limiting step in the fuel cell. Hence, understanding the factors controlling ORR and thereby the creation of high-performance ORR catalysts are essential for the development of efficient fuel cells.

Since Pt exhibits high ORR activity as well as high OER activity, the development of the miniaturization techniques, prediction of the activity by theoretical calculations, and the mechanism for Pt NCs have been studied extensively.<sup>42–44</sup> For example, Yamamoto *et al.* examined the ORR activity of fine Pt NCs (Pt<sub>n</sub> NC, *n* = 12–24) using dendrimer-encapsulated atomically-controlled Pt<sub>n</sub> NCs (Fig. 7).<sup>45</sup> The results demonstrated that Pt<sub>19</sub> NC exhibits the highest ORR activity (Fig. 7E). The edge site of Pt<sub>19</sub> has an ideal oxygen binding energy, which indicates that in addition to the electronic structure, the geometrical structure affects the ORR activity.<sup>46–48</sup>

Moreover, the use of Au<sub>n</sub>(SR)<sub>m</sub> NCs as catalysts for ORR has also attracted significant attention as an alternative to expensive Pt catalysts and to evaluate the catalytic reaction mechanism. Chen *et al.* reported that the ORR activity increases with a decrease of Au NC size (Au<sub>25</sub>(PET)<sub>18</sub> > Au<sub>38</sub>(PET)<sub>24</sub> > Au<sub>144</sub>(PET)<sub>60</sub>; Fig. 8A and B).<sup>49,50</sup> This increase is suggested to be due to the enhancement of the oxygen adsorption caused by increasing the proportion of surface atoms and shifting the d-band center associated with a decrease of Au NC size. Chakraborty and Dass *et al.* synthesized a series of 4-*tert*-butylbenzenethiolate (TBBT)-protected Au NCs and analyzed the ORR activity of Au NCs supported on single-walled carbon nanotubes.<sup>51</sup> The study on the reaction rate revealed that the ORR activity increases in the order of Au<sub>36</sub>(TBBT)<sub>24</sub> > Au<sub>133</sub>(TBBT)<sub>52</sub> > Au<sub>279</sub>(TBBT)<sub>84</sub> > Au<sub>28</sub>(TBBT)<sub>20</sub> (Fig. 8C and D). The same research group also used *tert*-butylthiolate (S-*t*Bu) as a ligand and showed that the ORR activity increases in the order of Au<sub>46</sub>(S-*t*Bu)<sub>29</sub> ≈ Au<sub>65</sub>(S-*t*Bu)<sub>29</sub> > Au<sub>30</sub>(S-*t*Bu)<sub>18</sub> > Au<sub>23</sub>(S-*t*Bu)<sub>16</sub> in the case of S-*t*Bu-protected Au NCs.<sup>52</sup>

In addition to the NC size, the control of charge state of NCs is also a crucial factor for obtaining high activity. For example, the negatively charged Au<sub>25</sub>(PET)<sub>18</sub> NC shows higher activity in the production of H<sub>2</sub>O<sub>2</sub>, which is a two-electron reduction reaction, than the neutral Au<sub>25</sub>(PET)<sub>18</sub> NC (Fig. 8E and F).<sup>53,54</sup> Since H<sub>2</sub>O<sub>2</sub> is a useful raw material for a variety of chemical products, the development of a highly selective H<sub>2</sub>O<sub>2</sub> production method is of importance. Likewise, the interaction with the substrate also requires consideration. Pt or Au NCs supported on various substrates, such as indium tin oxide (ITO)<sup>55</sup> and reduced graphene oxide (rGO) sheets<sup>56</sup> show outstanding electrocatalytic performance in ORR, which was found to be originated in the interaction between metal NC and the substrate.

### 2.3. Photocatalytic application for water splitting

Artificial photosynthesis, which has attracted significant attention in recent years, is an ultimate energy production technique involving conversion of light into chemical energy. In 1972, Honda and Fujishima *et al.* discovered that water can be split into H<sub>2</sub> and O<sub>2</sub> by irradiating the titanium dioxide (TiO<sub>2</sub>) photocatalyst with ultraviolet light.<sup>57</sup> Utilizing this method allows



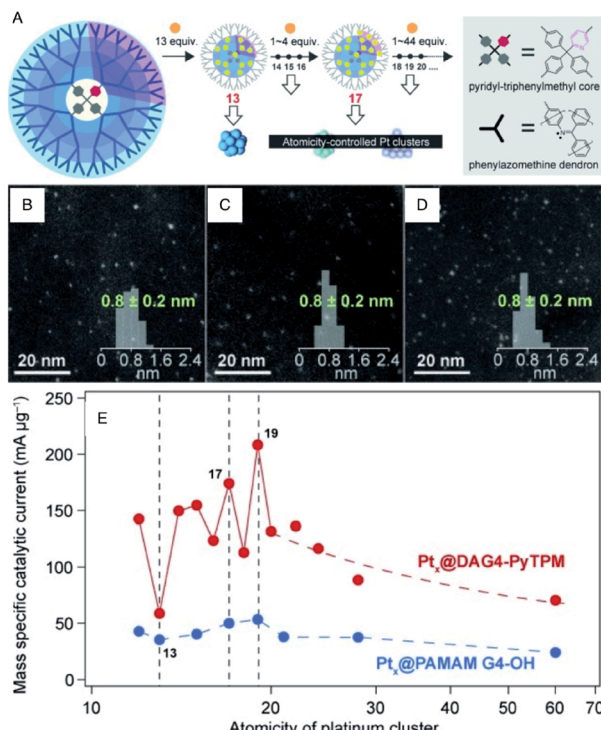


Fig. 7 (A) Illustration of the precise synthesis method of atomicity precise Pt NCs using a dendrimer reactor. HAADF-STEM images of (B) Pt<sub>13</sub>, (C) Pt<sub>17</sub> and (D) Pt<sub>19</sub> NCs. (E) Variations of the mass ORR activity vs. the atomicity of the Pt NCs. Panels (a)–(e) are reproduced with permission from ref. 45. Copyright 2015 Wiley-VCH.

efficient generation of H<sub>2</sub> as an energy source using abundant water, without the production of carbon dioxide. In the photocatalytic water splitting reaction, the catalyst comprises a photocatalyst, which absorbs light, and a cocatalyst whose role is to reduce the overpotential of HER and OER. Moreover, the photocatalyst uses light energy instead of electric energy as the driving force for HER or OER. Therefore, the position of the conduction and valence bands and the width of the bandgap are essential factors when considering the photocatalyst.

Highly active metal NCs in electrochemical HER and OER are effective cocatalysts in photocatalytic systems. The photocatalytic reaction involves several key steps: (1) generation of the e<sup>-</sup>–h<sup>+</sup> pair in the photocatalyst, (2) transfer of the e<sup>-</sup> and h<sup>+</sup> to the active sites, and (3) generation of H<sub>2</sub> and O<sub>2</sub> at the active sites. Here the cocatalyst greatly affects processes (2) and (3). The photodeposition and impregnation methods are typical approaches for loading cocatalysts on photocatalysts. They offer several advantages, such as the formation of fine metal particles directly on the photocatalyst. However, the disadvantages of these methods include large size dispersibility.

It is possible to load the controlled NC on photocatalyst and thereby to deepen the understanding on the effect of cocatalyst size on the photocatalytic activity when using an ultra-high vacuum apparatus. Heiz, Feldmann, and Jäckel *et al.* loaded a series of atomically precise Pt NCs (Pt<sub>8</sub>, Pt<sub>22</sub>, Pt<sub>34</sub>, Pt<sub>46</sub>, Pt<sub>68</sub>) on cadmium sulfide (CdS) nanorod utilizing an ultra-high vacuum apparatus (Fig. 9A and B).<sup>58,59</sup> They investigated the water-

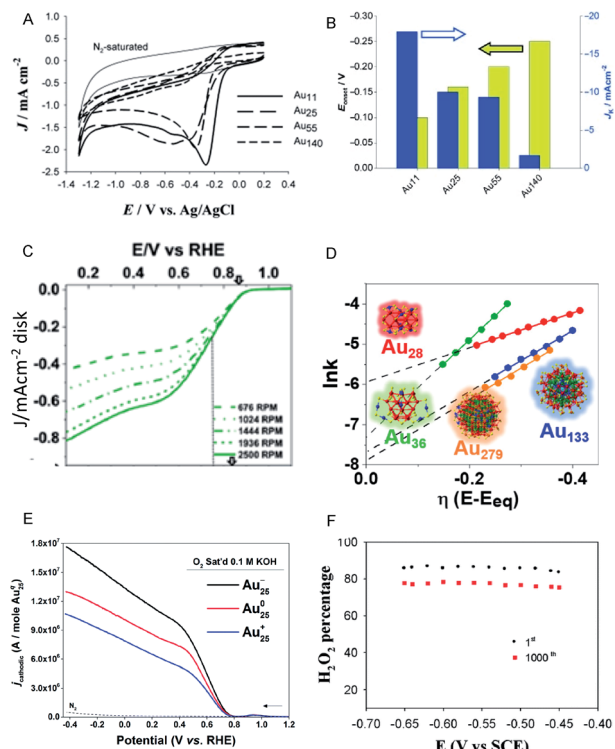


Fig. 8 (A) Cyclic voltammograms of the Au<sub>x</sub>/glassy carbon (GC) electrodes (x = 11, 25, 55 and 140) saturated with O<sub>2</sub> and of the Au<sub>11</sub>/GC electrode saturated with N<sub>2</sub> (thin solid curve). (B) Current density and overpotential of ORR activity with each size of Au NCs calculated from (A). (C) Rotating-disk voltammograms recorded for ORR activity by Au<sub>36</sub>(TBBT)<sub>24</sub> NCs/GC electrode at different rotation rates. (D) Reaction rate constant ln(k) vs. overpotential E plots with each size of Au NCs calculated from (C). (E) Rotating-ring-disk voltammograms with 1600 rpm rotation rate. (F) Percentage (or selectivity) of H<sub>2</sub>O<sub>2</sub> using with Au<sub>25</sub><sup>-</sup>, Au<sub>25</sub><sup>0</sup>, and Au<sub>25</sub><sup>+</sup> NCs. Panels (a) and (b) are reproduced with permission from ref. 49. Copyright 2009 Wiley-VCH. Panels (c) and (d) are reproduced with permission from ref. 51. Copyright 2018 American Chemical Society. Panel (e) is reproduced with permission from ref. 54. Copyright 2014 Royal Society of Chemistry. Panel (f) is reproduced with permission from ref. 53. Copyright 2014 Royal Society of Chemistry.

splitting activity of the resulting photocatalysts (Pt NC/CdS) and consequently revealed that Pt<sub>46</sub>/CdS exhibits the highest activity (Fig. 9C). In the NC region, the bandgap increases with a decrease of the NC size due to the quantum size effect. It was also reported that the control of the lowest unoccupied molecular orbital (LUMO) position of the cocatalyst by controlling the NC size is of great importance for the effective electron transfer from the photocatalyst to the cocatalysts. Furthermore, the group demonstrated that the LUMO position must be lower than the conduction band of the semiconductor photocatalysts and higher than the reduction potential of HER (Fig. 9D).

As well as investigation into electrochemical properties of HER and OER, research on photocatalytic water splitting is rapidly progressing also for Au<sub>n</sub>(SR)<sub>m</sub> NCs. Negishi and Kudo *et al.* developed a photocatalytic system comprising atomically precise Au<sub>25</sub> NC and the BaLa<sub>4</sub>Ti<sub>4</sub>O<sub>15</sub> photocatalyst (Fig. 10).<sup>60</sup> In this study, the atomically precise Au<sub>25</sub> NC was loaded on the

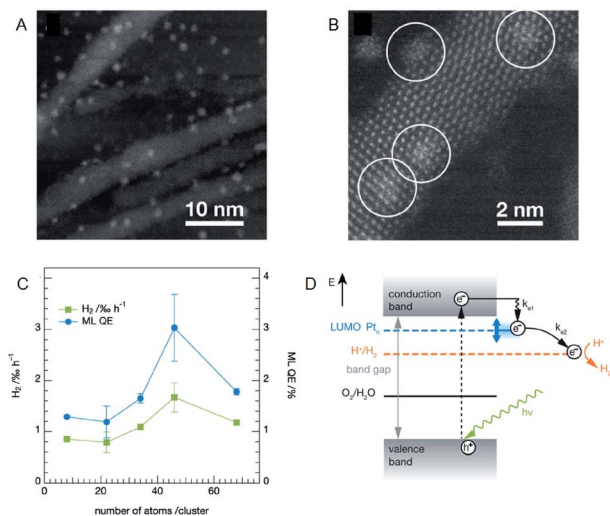


Fig. 9 (A) and (B) HAADF-STEM images of CdS nanorods decorated with Pt NCs at different magnification. (C) Photocatalytic activity of the CdS nanorods decorated with size-selected Pt NCs as a function of cluster size. (D) Reaction pathways for the photocatalytic H<sub>2</sub> evolution in CdS with Pt NCs. Panels (a)–(d) are reproduced with permission from ref. 58. Copyright 2013 American Chemical Society.

photocatalyst by adsorbing glutathionate (SG)-protected Au<sub>25</sub> NC on BaLa<sub>4</sub>Ti<sub>4</sub>O<sub>15</sub> and subsequently eliminating the SG ligands by calcination. TEM analysis of the products confirmed that NC-size change barely occurred during the calcination. The resulting Au<sub>25</sub>/BaLa<sub>4</sub>Ti<sub>4</sub>O<sub>15</sub> composite generates both H<sub>2</sub> and O<sub>2</sub> in a stoichiometric ratio upon light irradiation and the catalytic activity is 2.6 times higher than that of Au NP loaded-BaLa<sub>4</sub>Ti<sub>4</sub>O<sub>15</sub> (Fig. 10A). The same group also revealed that the smaller the particle size, the higher the activity (Fig. 10B). In their more recent study, it was

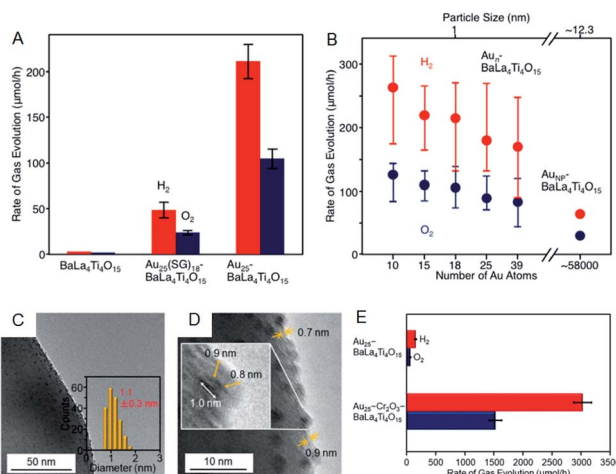


Fig. 10 Effect of (A) ligands protection and (B) cluster size on the rates of photocatalytic activity for water splitting studied using Au<sub>n</sub>/BaLa<sub>4</sub>Ti<sub>4</sub>O<sub>15</sub> ( $n = 10\text{--}39$ ) and Au NPs/BaLa<sub>4</sub>Ti<sub>4</sub>O<sub>15</sub>. (C) TEM image. (D) High resolution-TEM image. (E) Rates of photocatalytic activity for water splitting of Au<sub>25</sub>–Cr<sub>x</sub>O<sub>y</sub>/BaLa<sub>4</sub>Ti<sub>4</sub>O<sub>15</sub>. Panels (a) and (b) are reproduced with permission from ref. 60. Copyright 2015 American Chemical Society. Panels (c)–(e) are reproduced with permission from ref. 61. Copyright 2018 American Chemical Society.

described that the ORR, which is a reverse reaction, can be suppressed by coating the Au<sub>25</sub> NC with Cr<sub>2</sub>O<sub>3</sub>, and thereby the activity was improved by 19-fold compared to the non-coated Au<sub>25</sub>/BaLa<sub>4</sub>Ti<sub>4</sub>O<sub>15</sub> (Fig. 10C–E).<sup>61</sup> The cocatalysts with high HER and OER activities typically display good activity in HOR and ORR.<sup>62,63</sup> Overall, as shown in this study, the control of the reverse reaction is an important factor for improving the activity.

The photocatalytic activity could also be modulated by heteroatom doping on the cocatalysts. Negishi and Yamazoe *et al.* demonstrated that Pd doping on Au<sub>25</sub> NC reduces the water-splitting activity, whereas Pt doping on Au<sub>25</sub> NC enhances it (Fig. 11A–F).<sup>64</sup> Yang *et al.* also examined the effect of heteroatom doping on the photocatalytic activity of PtAg<sub>24</sub>-loaded graphitic carbon nitride (PtAg<sub>24</sub>/g-C<sub>3</sub>N<sub>4</sub>).<sup>65</sup> They revealed that PtAg<sub>24</sub>/g-C<sub>3</sub>N<sub>4</sub> shows higher activity for photocatalytic H<sub>2</sub> production than Ag<sub>25</sub>/g-C<sub>3</sub>N<sub>4</sub> (Fig. 11G and H). In addition to the above studies, there are several reports on water-splitting photocatalytic activity using composites including metal NCs, such as graphitic carbon nitride nanosheets carrying mercaptosuccinic acid-protected Ag<sub>9</sub> NC,<sup>66</sup> TiO<sub>2</sub> carrying SG-protected Au NC, *etc.*<sup>67,68</sup>

#### 2.4. Photosensitization for solar cell applications

Solar power generation systems, which directly convert light energy into electricity, continue to be important renewable energy sources and are the key components of the world's technological advancement. A photoelectrode cell, commonly known as the solar cell, comprises a light absorption layer, which generates e<sup>-</sup>–h<sup>+</sup> pairs, and a working electrode/counter electrode that independently take out e<sup>-</sup> and h<sup>+</sup>. The material used for the light absorption layer must effectively absorb light in the visible range, constituting approximately 50% of sunlight. In this respect, bulk gold reflects light due to a large number of free electrons. However, with the decreasing size of the NC, the number of electrons decreases, and discrete energy levels appear. Hence, a metal NC has a HOMO–LUMO gap similar to that of a molecule and exhibits light absorption in the visible to the near-infrared (NIR) region.

Tatsuma and Sakai previously demonstrated that metal NCs can be used for the light absorption layer in solar cells.<sup>69</sup> They produced a photoelectrode in which a TiO<sub>2</sub> electrode was coated with a series of SG-protected Au NC of various sizes (Au NC/TiO<sub>2</sub>). When hydroquinone was used as an electron donor, a photo-response was observed (Fig. 12A and B) and its photocurrent behavior was consistent with photocurrent action spectrum and absorption spectrum (Fig. 12C and D). These results indicate that an electron is excited and promoted from the HOMO to the LUMO by photoirradiation in Au NC and that the photoexcited electron of LUMO is transferred to the CB of TiO<sub>2</sub>. In this way, the Au NC functions like a dye in dye-sensitized solar cells (DSSCs). The same research group observed the generation of photovoltaic power even when the other element NCs (Ag, Pt and Pd NCs) were employed.<sup>70,71</sup> In addition, various other metal and alloy cluster sensitized solar cells have been reported by a number of research groups.<sup>72–74</sup>

Regarding the solar cells, Kamat *et al.* achieved a high external quantum efficiency (IPCE) of 70% at 400–425 nm by

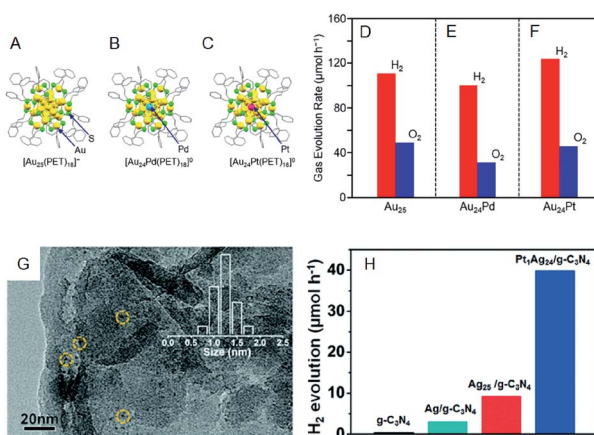


Fig. 11 Geometrical structures of (A)  $\text{Au}_{25}(\text{PET})_{18}$ , (B)  $\text{Au}_{24}\text{Pd}(\text{PET})_{18}$ , and (C)  $\text{Au}_{24}\text{Pt}(\text{PET})_{18}$ . Rates of photocatalytic activity for water splitting with  $\text{Au}_{24}\text{M}-\text{BaLa}_4\text{Ti}_4\text{O}_{15}$  for M = (A) Au, (E) Pd, and (F) Pt. (G) TEM image of  $\text{PtAg}_{24}/\text{g-C}_3\text{N}_4$ . (H) The rates of photocatalytic activity of  $\text{PtAg}_{24}/\text{g-C}_3\text{N}_4$ ,  $\text{Ag}_{25}/\text{g-C}_3\text{N}_4$ ,  $\text{Ag}/\text{g-C}_3\text{N}_4$ , and  $\text{g-C}_3\text{N}_4$ . Panels (a)–(f) are reproduced with permission from ref. 64. Copyright 2019 American Chemical Society. Panel (g) and (h) are reproduced with permission from ref. 65. Copyright 2017 Royal Society of Chemistry.

using a Co(bpy) redox pair ( $\text{Co}(\text{bpy})_3(\text{PF}_6)_2/\text{Co}(\text{bpy})_3(\text{PF}_6)_3$ ) in SG-protected Au NC/TiO<sub>2</sub> system (Fig. 13).<sup>75</sup> This value compares favorably even with the CdS-based quantum dot solar cells. The power conversion efficiency (PCE) was 2.36% at maximum, indicating that metal NCs can act as a high-performance sensitizer in sensitized solar cells. Bang, Kang, and Lee *et al.* achieved a PCE value as high as 3.8% when investigating SG-protected  $\text{Au}_{18}$  NC/TiO<sub>2</sub> solar cells using the  $\text{I}^-/\text{I}^{3-}$  redox pair (Fig. 14).<sup>76</sup> They reported that  $\text{Au}_{18}$  NC barely underwent exciton recombination and absorbed light in a wide

wavelength range, resulting in high solar cell characteristics (Fig. 14A–C).

However, to improve the stability of the system, other ligand-protected metal NCs should be used. Pradeep *et al.* compared the photovoltaic performance of solar cells using various ligand-protected metal NCs, such as bovine serum albumin, TBBT, and 4-mercaptopbenzoic acid.<sup>73</sup> They reported that the  $\text{Au}_{30}$  NC protected with bovine serum albumin has highest PCE (0.35%).

In the described systems, there is a correlation between the expansion of the light absorption wavelength range of the metal NCs and the decrease in opening photovoltage accompanying the bandgap decrease. To further improve the PCE, combination with other light-absorbing materials is required. DSSC using a squalene dye as the co-sensitizer was reported to provide a PCE of 4%,<sup>77</sup> and a maximum PCE of 9.15% (ref. 78) by incorporating  $\text{Au}_{38}$  clusters in organic thin-film solar cells.

### 3. Photosensitization of metal NCs for therapeutic applications

#### 3.1. Photo-based therapeutic applications of water-soluble metal NCs

Water-soluble noble metal (such as Au and Ag) NCs are composed of a metal core with several to a few hundred atoms, capped by water-soluble ligands such as amino acids, peptides, proteins, deoxyribonucleic acid (DNA), and hydrophilic thiolate ligands with different functional groups (e.g.,  $-\text{COOH}$ ,  $-\text{OH}$ , and  $-\text{NH}_2$ ). These water-soluble metal NCs exhibit unique physico-chemical properties including high photostability, low toxicity, and luminescence. In addition, the good penetration of such ultra-small metal NCs into the cells, the ability to target tumors through

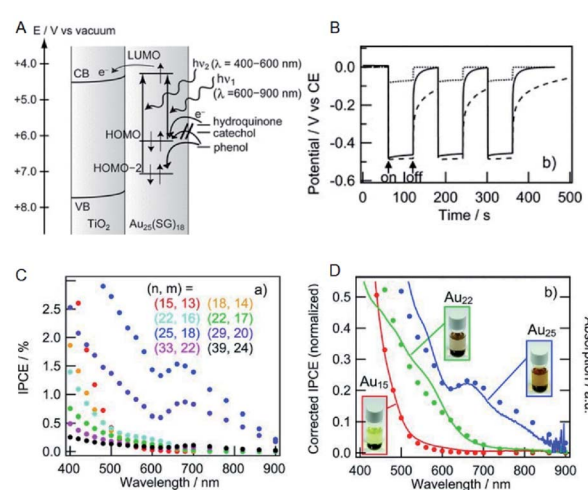


Fig. 12 (A) Mechanism of Au NCs sensitized solar cells. (B) Photopotential and (C) incident photons conversion efficiency vs. irradiation light wavelength (incident power conversion efficiency (IPCE) spectra) of Au NCs sensitized solar cells. (D) Normalized IPCE spectra and absorption spectra of Au NCs sensitized solar cells. Panels (a)–(d) are reproduced with permission from ref. 69. Copyright 2010 Wiley-VCH.

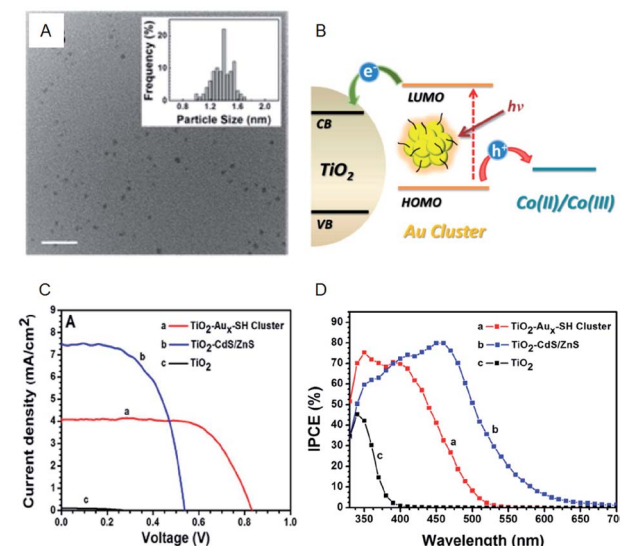


Fig. 13 (A) TEM image of  $\text{Au}_x$ -SG cluster. Scale bar shows the length of 10 nm. (B) Schematic of the working principle of metal-NC-sensitized solar cells. (C)  $J$ – $V$  characteristics. (D) IPCE spectra of  $\text{TiO}_2$  modified with  $\text{Au}_x$ -SH cluster,  $\text{TiO}_2$  modified with CdS/ZnS and  $\text{TiO}_2$  electrodes. Panels (a)–(d) are reproduced with permission from ref. 75. Copyright 2013 American Chemical Society.



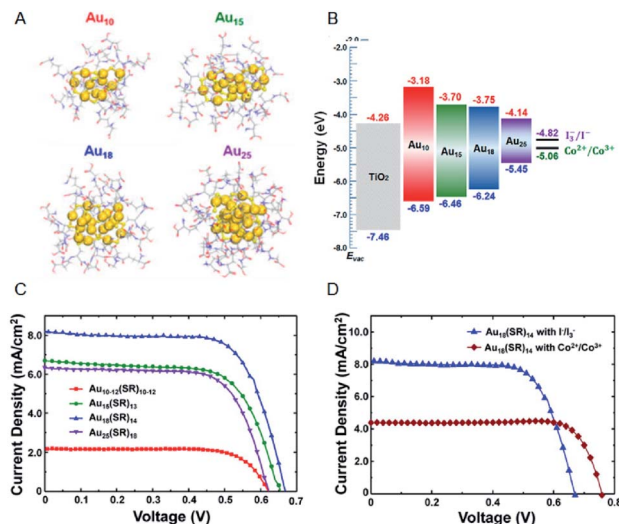


Fig. 14 (A) Geometrical structures of  $\text{Au}_x(\text{SG})_y$  NCs ( $x = 10, 15, 18$  and  $25$ ). (B) Energy diagrams of the  $\text{Au}_x(\text{SG})_y$  NCs sensitized solar cells.  $J$ – $V$  characteristics of (C)  $\text{Au}_x(\text{SG})_y$  NCs sensitized solar cells ( $x = 10, 15, 18$  and  $25$ ) with  $\text{I}^-/\text{I}^{3-}$  redox pair and (D)  $\text{Au}_{18}(\text{SG})_{14}$  NCs sensitized solar cells with  $\text{I}^-/\text{I}^{3-}$  or  $\text{Co}^{2+}/\text{Co}^{3+}$  redox pair. Panels (a)–(d) are reproduced with permission from ref. 76. Copyright 2016 American Chemical Society.

proper surface modification, and their superior renal clearance make the water-soluble metal NCs promising materials for utilization in the field of biomedicine, *e.g.*, bioimaging, sensing, drug delivery, and diagnostic and therapeutic applications.

Cancer is a class of common life-threatening diseases, understanding of which is incomplete, despite significant efforts and extensive research. Developed therapies against cancer include chemotherapy (chemo-T), radiotherapy (RT), surgery, immunotherapy, NPs-based therapy, photothermal therapy (PTT), and PDT.<sup>79</sup> Among them, PDT is considered clinically reliable and non-invasive. In this method reactive oxygen species (ROS) generated by a photoexcited photosensitizer kill the tumor cells.

Traditional PDT utilizes organic photosensitizers with organic dye molecules such as porphyrin and its derivatives, chlorin e6, methylene blue, rose bengal, eosin Y, and indocyanine green. However, organic photosensitizers suffer from common drawbacks including low water-solubility, poor selectivity, toxicity, and photo-instability. Meanwhile, known inorganic photosensitizers include quantum dots, silicon nanocrystals, fullerene ( $\text{C}_{60}$ ), and metal NPs.<sup>80–83</sup> More recently,  $\text{Au}_n(\text{SR})_m$  NCs have been considered as promising photosensitizers for PDT. Their electronic structures can be optimized for efficient singlet oxygen ( ${}^1\text{O}_2$ ) production using atomically precise size control. Several fundamental properties of the  $\text{Au}_n(\text{SR})_m$  NCs are also desirable for PDT, such as good biocompatibility in dark conditions, photosensitization under near-infrared light irradiation, good resistance to photo-bleaching, and target specificity *via* surface modification. The following section focuses on the photosensitizing ability of  $\text{Au}_n(\text{SR})_m$  NCs toward PDT applications. A number of recent

reviews on other biomedical applications of metal NCs have also been published.<sup>15–17</sup>

### 3.2. Basic principle of photosensitization for PDT

Upon absorbing the appropriate light, the photosensitizer transitions from the ground singlet state ( $\text{S}_0$ ) to the excited singlet state ( $\text{S}_1$ ). Through non-radiative transition, it subsequently changes the multiplicity from  $\text{S}_1$  to a triplet state ( $\text{T}_1$ ) *via* intersystem crossing (ISC). The photosensitizer in the  $\text{T}_1$  state can then decay *via* two distinctive processes: Type I and Type II (Fig. 15). In Type I, the excited photosensitizer undergoes single-electron transfer with the substrate to produce a radical or a radical ion, such as hydroxyl radical ( $\cdot\text{OH}$ ) and superoxide ( $\text{O}_2^{\cdot-}$ ). These highly reactive radical species can further react with biological substrates to modify their structure and/or function. In the Type II process, however,  ${}^1\text{O}_2$  produced *via* the energy transfer from the photosensitizer to oxygen, readily reacts with biological molecules (*e.g.*, lipids, proteins, and DNA), which are the main components of cells and nuclear membranes. The majority of the effective photosensitizers are characterized by high quantum yields of their  $\text{T}_1$  state, since a relatively longer living  $\text{T}_1$  state allows more chance for energy and/or electron transfer. Thus, ROS such as  $\text{O}_2^{\cdot-}$ ,  $\cdot\text{OH}$ , and  ${}^1\text{O}_2$  are key species in the PDT process.<sup>84,85</sup>

The lifetime of  ${}^1\text{O}_2$  in most biological environments is in the range of a few microseconds. Thus,  ${}^1\text{O}_2$  produced from Type II photosensitization can affect biological substrates within a moderate distance from the photosensitizer itself (0.02–0.15  $\mu\text{m}$ ). In contrast,  $\cdot\text{OH}$  produced in Type I photosensitization is highly reactive and interacts with biological molecules within a range of less than 5 nm, restricting its effects to the location where it is produced.<sup>84,85</sup> Thus,  ${}^1\text{O}_2$  formed from the Type II reaction is thought to be primarily responsible for the biological effect in PDT.

The direct confirmation of  ${}^1\text{O}_2$  generation in photosensitization reactions comes from detecting phosphorescence at around 1270 nm resulting from the spontaneous decay of  ${}^1\text{O}_2$  to its ground state. Other methods of  ${}^1\text{O}_2$  detection are based on analyzing the spectral change of a probe molecule upon its interaction with  ${}^1\text{O}_2$ , using electron spin resonance (ESR), UV-vis absorption, or fluorescence. The various  ${}^1\text{O}_2$  detection techniques and their probes are summarized in Table 2.

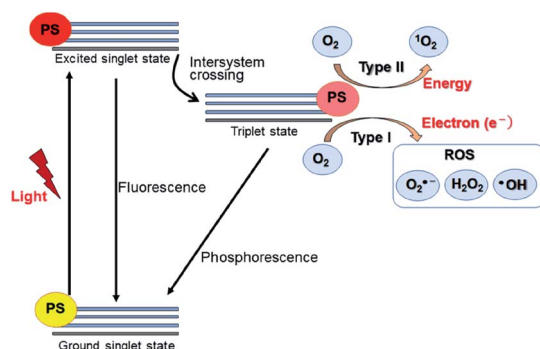


Fig. 15 Schematic Jablonski's diagram of Type I and Type II reactions in PDT. PS: photosensitizer.



$^1\text{O}_2$  scavengers can also be used to confirm the  $^1\text{O}_2$  generation. Azide ion and histidine are often utilized as quenchers for  $^1\text{O}_2$ . They rapidly and preferentially interact with  $^1\text{O}_2$  and convert it to the ground state  $\text{O}_2$  before reacting with any other molecules in the system. Further confirmation of  $^1\text{O}_2$  can be obtained by replacing water with deuterated water, which extends the lifetime of  $^1\text{O}_2$  by as much as 15-fold.

### 3.3. Au NC-based photosensitizer for PDT

In previous studies, protein-stabilized Au NCs and Au NCs embedded in polymer matrix were reported to produce  $^1\text{O}_2$  upon photoexcitation at 330 and 532 nm (UV and visible light, respectively).<sup>86,87</sup> Following these reports, Kawasaki and Jin *et al.* described the formation of  $^1\text{O}_2$  through direct sensitization of  $\text{Au}_{25}(\text{SR})_{18}$  ( $\text{H-SR}$  = phenylethanethiol or captopril) under visible/NIR light (532, 650, and 808 nm) irradiation.<sup>88</sup> The generation of  $^1\text{O}_2$  by photoexcited  $\text{Au}_{25}(\text{SR})_{18}$  was confirmed by observation of the  $^1\text{O}_2$  emission at approximately 1270 nm,  $^1\text{O}_2$ -selective probes, and the use of a  $^1\text{O}_2$  quencher.<sup>88</sup> The larger HOMO-LUMO gap of  $\text{Au}_{25}(\text{SR})_{18}$  NCs (1.3 eV) than the energy of  $^1\text{O}_2$  (0.97 eV), the long lifetime of the electronic excitations, and the well-defined  $\text{O}_2$  adsorption sites are suggested to be the key factors promoting the energy transfer from the  $\text{Au}_{25}(\text{SR})_{18}$  NCs to molecular oxygen resulting in the formation of  $^1\text{O}_2$ . Photodynamic activity of water-soluble  $\text{Au}_{25}(\text{Capt})_{18}$  NCs toward cancer cells under NIR light (808 nm) was also demonstrated (Fig. 16A). Moreover, Miyata and Miyaji *et al.* developed  $\text{Au}_{25}(\text{-Capt})_{18}$  NCs exhibiting photodynamic activity toward oral bacteria (Fig. 16B).<sup>89</sup>

The following section includes discussion of several strategies to improve the  $^1\text{O}_2$  generation efficiency and PDT activity of Au NCs by using: (i) atomically precise size control, (ii) NIR activation for deep-tissue treatments, (iii) aggregation-induced emission (AIE), (iv) resonance energy transfer (RET), and (v) forming nanocomposites with other nanomaterials for multimodal synergistic therapy (Fig. 17).

**3.3.1. Atomically precise size control of Au NC (or Ag NC)-based photosensitizers.** Au NCs with different sizes and ligands have been used to improve the  $^1\text{O}_2$  generation efficiency, depending on the size of NCs at the atomic level. For example,

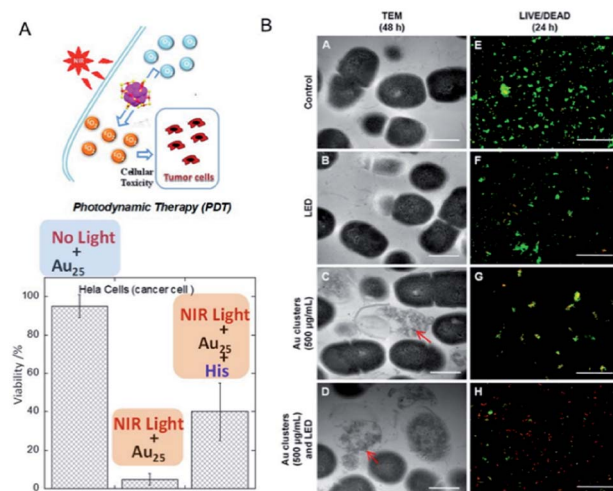


Fig. 16 Photodynamic action of  $\text{Au}_{25}(\text{Capt})_{18}$  NCs. (A) HeLa cancer cells under NIR light in the presence/absence of histidine, a  $^1\text{O}_2$  scavenger. (B) TEM images of *Streptococcus mutans* after 48 h incubation, and LIVE (green)/DEAD (red) results of *S. mutans* after 24 h incubation. Panel (a) is reproduced with permission from ref. 88. Copyright 2014 American Chemical Society. Panel (b) is reproduced with permission from ref. 89. Copyright 2017 Dove Medical Press Ltd.

$\text{Au}_{38}(\text{PET})_{24}$  NCs have been shown to be less effective compared to  $\text{Au}_{25}(\text{PET})_{18}$ ,<sup>88</sup> since the optical gap of the former ( $\sim 0.9$  eV) is smaller than the energy of  $^1\text{O}_2$  (0.97 eV). Talavera *et al.* examined the excited state properties of tetraoctyl ammonium (TOA) capped  $\text{Au}_{10-12}$  (SG) NCs in toluene.<sup>90</sup> The Au NCs exhibited a relatively long-lived triplet excited state, which originated from the ligand to the charge transfer state between the SG shell and the Au core. The quantum yields of  $^1\text{O}_2$  ( $\sim 0.13$ ) and the triplet excited state ( $\sim 0.15$ ) were evaluated by 1,3-diphenylisobenzofuran (DPBF, a  $^1\text{O}_2$ -selective probe) and triplet-triplet absorption spectra. Ho-Wu *et al.* investigated the size effect of Au NCs on the  $^1\text{O}_2$ -generation efficiency from  $\text{Au}_{25}(\text{SG})_{18}$ ,  $\text{Au}_{144}(\text{C}_6)_{60}$ , and plasmonic Au NPs ( $\sim 40$  nm).<sup>91</sup> The  $\text{Au}_{144}$  NCs had a much higher  $^1\text{O}_2$  generation rate ( $^1\text{O}_2/\text{NC}/\text{min} = \sim 3.2$ ) than  $\text{Au}_{25}$  NCs ( $\sim 0.077$ ). The following order for the  $^1\text{O}_2$  generation rate was reported:  $\text{Au}_{144} > \text{Au}_{25} \gg \text{Au NPs}$  (Fig. 18A).

Table 2 Singlet oxygen ( $^1\text{O}_2$ ) detection methods

Method	Probe	Detection
Phosphorescence	$^1\text{O}_2$	Phosphorescence of $^1\text{O}_2$ at 1270 nm
UV-vis spectroscopy	9,10-Diphenyl-anthracene (DPA)	Decrease peak at 355 nm
UV-vis spectroscopy	9,10-Anthracenediyl-bis(methylene) dimalonic acid (ABDA)	Decrease peak at 382 nm
UV-vis spectroscopy	9,10-Anthracenedipropionic acid (ADPA)	Decrease peak at 400 nm
UV-vis spectroscopy	Anthracene-9,10-bisethanesulfonic acid (AES)	Decrease peak at 360, 378 and 400 nm
UV-vis spectroscopy	1,3-Diphenyl-isobenzofuran (DPBF)	Decrease peak at 410 nm
UV-vis spectroscopy	<i>p</i> -Nitrosodimethylaniline imidazole (RNO method)	Decrease peak at 440 nm
Fluorescence	Singlet oxygen sensor Green (SOSG)	Increased fluorescence at 540 nm
Fluorescence	Methotrexate (MTX)	Increased fluorescence at 450 nm
ESR	2,2,6,6-Tetramethyl-piperidine (TEMP)	Change in enhanced permeability and ESR spectrum



## Strategies of Au NCs to improve ${}^1\text{O}_2$ generation for PDT applications

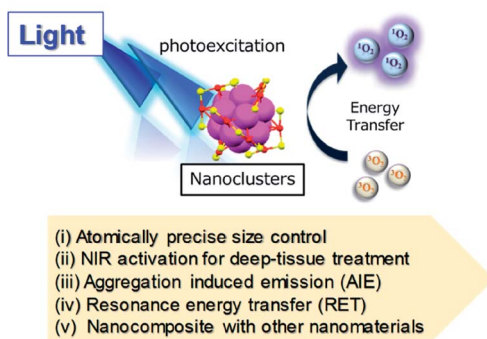


Fig. 17 Schematic illustration of different approaches to improve  ${}^1\text{O}_2$  generation from Au NCs for PDT.

The superior  ${}^1\text{O}_2$  generation with  $\text{Au}_{144}$  was attributed to the combination of a high absorption cross section relative to the volume and a high triplet excited state population *via* core-localized plasmon resonance.

Compared to the Au NC-based photosensitizers, reports on Ag NC-based photosensitizers are limited due to their low photostability.<sup>92</sup> Yu *et al.* examined bovine serum albumin (BSA)-protected  $\text{Ag}_{13}$  NC as a photosensitizer. Due to a large population in the triplet state, the BSA- $\text{Ag}_{13}$  NCs showed high

${}^1\text{O}_2$  generation quantum efficiency ( $\sim 1.26$  using rose bengal as the standard).<sup>93</sup> Owing to the good cellular uptake and high  ${}^1\text{O}_2$  generation efficiency, the BSA- $\text{Ag}_{13}$  can effectively kill the MCF-7 breast cancer cells following uptake and white light treatment (Fig. 19B). Tominaga and Kawasaki *et al.* demonstrated that  $\text{Ag}_7(\text{MBISA})_6$  (MBISA = 2-mercaptop-5-benzimidazolesulfonic acid sodium salt) NCs also generate  ${}^1\text{O}_2$  with high efficiency under white light irradiation. The following order was suggested for the  ${}^1\text{O}_2$  generation efficiency on different Ag NCs:  $\text{Ag}_7(\text{MBISA})_6 > \text{BSA-}\text{Ag}_{13} > \text{Ag}_{75}(\text{SG})_{40} > \text{Ag}_{35}(\text{SG})_{18} > \text{BSA-}\text{Ag}_8$  (not detected).<sup>94</sup>

**3.3.2. NIR activation of Au NC photosensitizers for deep-tissue treatments.** NIR light (700–950 nm, also named the NIR-I window) has much deeper tissue penetration compared to visible light for cancer PDT. Ho-Wu *et al.* utilized two-photon excited  $\text{Au}_{25}(\text{SR})_{18}$  from a pulsed 800 nm laser to generate  ${}^1\text{O}_2$  and trigger PDT.<sup>91</sup> The two-photon NIR-triggered PDT was more effective in live cells compared to the one-photon excitation. More recently, the “NIR-II” window (1000–1700 nm) has also been attracting interest because of the decreased light scattering by tissues, lower background autofluorescence, and deeper tissue penetration.<sup>95,96</sup> Vankayala *et al.* reported a mercaptoundecanoic acid (MUA)-protected Au NCs conjugated transactivator of transcription (TAT) peptide (peptide sequence: N-GRKKRRQRRR-C).<sup>97</sup> The TAT peptide–Au NCs not only produced  ${}^1\text{O}_2$  under NIR-II light (980 nm), but also acted as DNA nano-cargo to achieve high gene transfection efficiencies

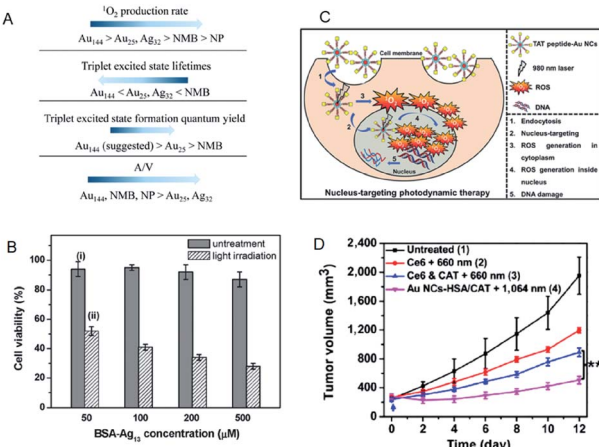


Fig. 18 (A) Summary of the photosensitizing properties of Au NCs, Ag NCs, Au NPs, and new methylene blue for producing  ${}^1\text{O}_2$ . (B) MTT assay histogram showing the viability of MCF-7 cancer cells treated with BSA- $\text{Ag}_{13}$  NCs at concentrations ranging from  $50$  to  $500 \times 10^{-6}$  M (Ag basis) with and without light irradiation. (C) Schematic of the PDT mechanism mediated by nucleus-targeting TAT peptide–Au NCs (peptide sequence: TAT = N-GRKKRRQRRR-C). (D) NIR-II triggered PDT on tumors. Growth curves of large tumors in mice after different treatments: (1) untreated control; (2) Ce6 + 660 nm laser; (3) Ce6 + CAT + 660 nm laser; (4) AuNC@HSA/CAT + 1064 nm laser. Panel (a) is reproduced with permission from ref. 91. Copyright 2017 American Chemical Society. Panel (b) is reproduced with permission from ref. 93. Copyright 2016 Wiley-VCH. Panel (c) is reproduced with permission from ref. 97. Copyright 2015 Wiley-VCH. Panel (d) is reproduced with permission from ref. 98. Copyright 2018 Springer Nature.

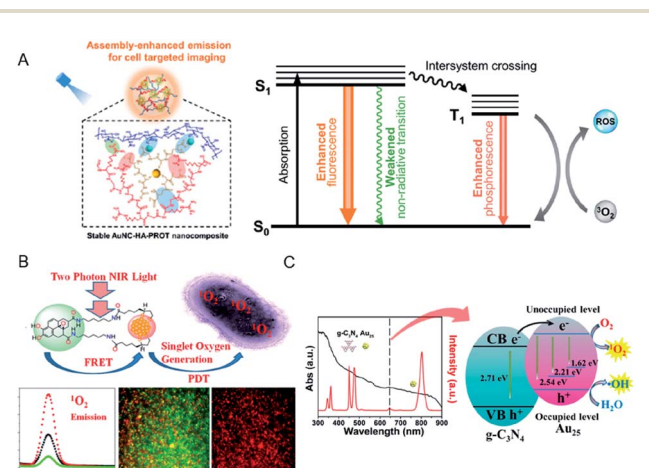


Fig. 19 (A) Schematic of the application of AuNC–hyaluronic acid (HA)–protein protamine (PROT) nanocomposites with enhanced emission and ROS generation through a self-assembly approach. (B) FRET-based two-photon excited theranostic nanoplatform using Au NCs attached to GQD for two-photon imaging and two-photon induced PDT killing of MDRB.  ${}^1\text{O}_2$  emissions under two-photon excitation at  $\sim 1270$  nm on the nanoplatform. (C) UV-vis absorption spectrum (black) and emission spectrum (red) of  $\text{Tm}^{3+}$ –activated up-conversion NPs (UCNPs)@g-C<sub>3</sub>N<sub>4</sub>–Au<sub>25</sub>–PEG upon 980 nm NIR laser excitation, and schematic of the ROS generation mechanism. Panel (a) is reproduced with permission from ref. 106. Copyright 2019 American Chemical Society. Panel (b) is reproduced with permission from ref. 115. Copyright 2018 American Chemical Society. Panel (c) is reproduced with permission from ref. 118. Copyright 2017 American Chemical Society.



( $\approx 81\%$ ) in HeLa cells (Fig. 18C). Furthermore, Chen *et al.* developed NIR-II light-activated PDT using MUA-protected Au NCs.<sup>98</sup> The Au NCs were modified with human serum albumin and catalase (AuNC@HSA/CAT). The nanocomposite produced  $^1\text{O}_2$  upon NIR-II light excitation (1064 nm), which effectively inhibited tumor growth by deeper tissue penetration of the NIR-II light (Fig. 18D).

Recently, X-ray was also combined with Au NCs as “radiosensitizer” for cancer radiotherapy. The use of X-ray as the light source is most suitable for activating the Au NCs for deep-tissue cancer treatment and biomedical imaging applications, due to its nearly unlimited penetration depth in living tissues and organisms. An interesting review,<sup>99,100</sup> as well as various other recent publications<sup>101–103</sup> covering the applications of Au NCs as radiosensitizers are available.

**3.3.3. AIE-active Au NC-based photosensitizer.** A number of strategies to improve the  $^1\text{O}_2$ -generation efficiency have been proposed for organic photosensitizers. The incorporation of heavy atoms into the molecular structures is the most widely utilized approach. In particular, photosensitizers with the AIE photosensitizers property have recently attracted significant attention.<sup>104</sup> NPs with a dense core of AIE fluorogen show strong emission in the aggregate state due to the restriction of intramolecular motions. They could also be designed to possess efficient photosensitizing abilities in the aggregate state, by reducing the singlet-triplet gap of AIE photosensitizers for efficient ISC. Hikosou and Kawasaki *et al.* applied the AIE-active strategy for NCs of AuAg alloy to enhance the  $^1\text{O}_2$  generation.<sup>105</sup> The AuAg alloy NCs were encapsulated by chitosan self-assembly, resulting in inhibited energy dissipation through non-radiative pathways and enhanced the  $^1\text{O}_2$  generation. Xia *et al.* also reported SG-protected Au NCs embedded in a hyaluronic acid/protein protamine self-assembly (AuNC-HA-PROT). The AuNC-HA-PROT nanocomposite showed enhancement in both light emission and  $^1\text{O}_2$  generation by inhibiting energy dissipation through non-radiative pathways (Fig. 19A).<sup>106</sup> Results of *in vitro* experiments revealed that the AuNC-HA-PROT nanocomposite showed effective endocytosis of target MDA-MB-231 cancer cells, high PDT activity, as well as fluorescence imaging.

**3.3.4. FRET-mediated Au NC photosensitizer.** Förster RET (FRET) involves energy transfer from an excited molecular chromophore (the donor) to another chromophore (the acceptor).<sup>107,108</sup> The following factors are primarily required to cause FRET: (i) a spectral overlap between the fluorescence of the donor chromophore and the absorption of the acceptor chromophore, (ii) small distance between the donor and the acceptor (typically, 10–100 Å), and (iii) parallel orientations of the donor and the acceptor transition dipoles. Yamamoto and Kawasaki *et al.* applied FRET for a nanocomposite of BSA-Au NC and methylene blue (MB) (BSA-Au NC-MB) to enhance the  $^1\text{O}_2$  generation.<sup>109</sup> The BSA-Au NC-MB nanocomposite exhibited good overlap between the absorption spectrum of MB and the emission spectrum of BSA-AuNCs. This resulted in enhanced FRET-mediated  $^1\text{O}_2$  production by energy transfer from the Au NC (the donor) to the MB (the acceptor) in the nanocomposite. In the conjugate of  $\text{Ag}_7(\text{MBISA})_6$  and quinacrine (QC), Tominaga and

Kawasaki *et al.* reported that the QC acts as a donor chromophore, while the Ag NC plays the role of the acceptor chromophore in the FRET process.<sup>94</sup> The FRET-mediated conjugate of  $\text{Ag}_7(\text{MBISA})_6$  and QC caused a 2.3-fold increase in the  $^1\text{O}_2$  generation compared to that obtained with  $\text{Ag}_7(\text{MBISA})_6$  NC alone.

The use of chromophore ligands can control photo-functions of metal nanoparticles and metal NCs.<sup>110–113</sup> Two-photon absorption of ligand-protected metal NCs shows a nonlinear optical property that is attractive for applications such as biological imaging and PDT.<sup>114</sup> Vangara *et al.* demonstrated two-photon PDT under 860 nm NIR excitation for multiple drug resistance bacteria (MDRB) using a nanocomposite of  $\alpha$ -lipoic acid stabilized Au NCs and graphene quantum dots (GQDs) (Au NCs-GQDs nanocomposite),<sup>115</sup> where the GQDs with high NIR absorption act as two-photon donor-chromophores, while the Au NCs act as acceptors. Due to the FRET process between the Au NCs and the GQDs, the  $^1\text{O}_2$  generation capability of Au NCs-GQD nanocomposite enhanced tremendously, which was higher than that of rose bengal, which is an efficient organic photosensitizer ( $^1\text{O}_2$  quantum yield of rose bengal,  $\Phi_{\text{RB}} = 0.75$ ) (Fig. 19B). The Au NCs-GQDs nanocomposite allowed bright two-photon bioimaging and two-photon PDT against MDRB and carbapenem-resistant *Escherichia coli*.

The singlet fission (SF) is a photophysical process in which interaction between one singlet-excited state ( $S_1$ ) and ground state ( $S_0$ ) species generates two triplet-excited species ( $T_1 + T_1$ ).<sup>116</sup> The SF enables the maximum yield of triplet excitons to be 200% different from simple intersystem crossing (ISC). Saegusa and Hasobe *et al.* newly synthesized a series of mixed tetracene (TC)-protected Au NCs prepared from a TC-modified heterodisulfide with two different chain lengths, which achieved a high-yield SF ( $\Phi_{\text{SF}} = 90\%$ ) and individual triplet yields ( $\Phi_T = 160\%$ ).<sup>117</sup> High-yield and long-lived triplet excited states through SF-based metal NCs may be also used for PDT application.

Feng *et al.* fabricated a dual-photosensitizer nanocomposite by coating a mesoporous layer of graphitic-phase carbon nitride ( $\text{g-C}_3\text{N}_4$ ) on  $\text{Tm}^{3+}$ -activated up-conversion NPs (UCNPs), followed by attachment of  $\text{Au}_{25}(\text{MHA})_{18}$  (MHA = 6-mercaptophexanoic acid) and polyethylene glycol molecules (UCNPs@ $\text{g-C}_3\text{N}_4$ - $\text{Au}_{25}$ -PEG) for PDT and bioimaging under NIR light.<sup>118</sup> The higher PDT efficiency of this nanocomposite in comparison with any single modality was demonstrated by the increased ROS production *via* the energy transfer in the UCNPs@ $\text{g-C}_3\text{N}_4$ - $\text{Au}_{25}$ -PEG system when excited by NIR light (980 nm). In addition, the effective separation of photogenerated electron-hole pairs in the nanocomposite could also promote the production of  $\cdot\text{OH}$  (Fig. 19C) and, consequently, cancer cell death. The therapeutic efficacy of the nanocomposite in animal experiments and tissue section analysis demonstrated the ability to inhibit tumor growth without damaging the major organs.

**3.3.5. Au NC-based photosensitizers for hypoxic environment.** Photosensitizers with Type II mechanism (*i.e.*,  $^1\text{O}_2$  generation) are the majority for PDT applications; however, their therapeutic efficacy is dependent on the oxygen level in the targeted microenvironment. Meanwhile, the native microenvironment of many tumors is low in oxygen (*i.e.*, hypoxic), since the rapid tumor growth outpaces the oxygen supply. As a result,



the PDT efficiency is reduced in such hypoxic environments.<sup>119</sup> Several approaches for solving this challenge have been proposed:<sup>120</sup> (1) *in situ* generation of  $O_2$ , (2)  $O_2$  independent PDT (Type I PDT), and (3) multimodal synergistic therapy. In the first approach (*in situ*  $O_2$  generation),  $H_2O_2$  is catalytically decomposed to form  $O_2$  and water. In cancer cells, the levels of  $H_2O_2$  are usually larger than in healthy cells.<sup>121</sup> With this in mind, Chen *et al.* constructed a self-supply  $O_2$  system for PDT against hypoxic tumors using the nanocomposite of AuNC@HSA/CAT.<sup>98</sup> The AuNC@HSA/CAT could self-supply  $O_2$  for PDT as a consequence of its intrinsic catalase-like activity to decompose  $H_2O_2$  and form  $O_2$  (Fig. 20A). This resulted in greatly improved  $O_2$  generation and increased PDT efficacy for hypoxic cancer cells (Fig. 20B and C). Liu *et al.* also described self-supplying  $O_2$  through catalase-like activity of PAMAM dendrimer-encapsulated Au NCs (AuNCs-NH<sub>2</sub>) for hypoxic tumor PDT.<sup>122</sup> The AuNCs-NH<sub>2</sub> exhibited catalase-like activity in the physiological pH range (*i.e.*, 4.8–7.4), hence decomposed  $H_2O_2$  to self-supply  $O_2$ . The proposed mechanism was that in acidic solutions the protonated tertiary amine groups of dendrimers facilitate the pre-adsorption of OH on the metal surface, triggering the catalase-like reaction.

To overcome the hypoxia limitation in Type II PDT, an  $O_2$  independent Type I PDT has recently been developed, as these photosensitizers produce  $HO^\bullet$ .<sup>119,120</sup>  $HO^\bullet$  is a stronger oxidant than  $^1O_2$  and could react with virtually any biological molecule, including DNA, proteins, lipids, and carbohydrates (Fig. 21).<sup>123</sup> Yang *et al.* fabricated  $Au_{25}$  NCs anchored on black anatase  $TiO_{2-x}$  nanotubes ( $Au_{25}/B-TiO_{2-x}$  NTs) for Type I PDT.<sup>124</sup> Under NIR light, the  $Au_{25}/B-TiO_{2-x}$  NTs could achieve separation of the  $e^- - h^+$  pair, leading to the production of  $HO^\bullet$  and  $O_2^\bullet-$  radicals. *In vivo* and *in vitro* experiments demonstrated an obviously enhanced PDT effect of  $Au_{25}/B-TiO_{2-x}$  NTs. Cheng *et al.* also fabricated titanium dioxide NP-Au NCs-graphene heterogeneous nanocomposites to induce a large production of  $HO^\bullet$  and  $O_2^\bullet-$  radicals, which could serve as Type I PDT for B16F1 melanoma cells.<sup>125</sup>

**3.3.6. Multimodal synergistic *in vivo* therapy using Au NC-based photosensitizer.** The efficacy of PDT using Au NC-based photosensitizers can be enhanced by combination with other therapeutic modalities, such as conjugates with organic photosensitizers, chemo-T, RT, PTT, and targeted imaging. In this context, we focused on Au NC-based multimodal synergistic therapies, particularly PTT,<sup>88,126–128</sup> chemo-T,<sup>129–131</sup> and conjugates with organic photosensitizers.<sup>132,133</sup>

He *et al.* assembled  $Au_{25}(Capt)_{18}$  onto mesoporous silica-coated Nd<sup>3+</sup>-sensitized up-conversion NPs (UCNPs@MS-Au<sub>25</sub>) to form a multifunctional platform for photoacoustic (PA) imaging and dual phototherapy (PTT/PDT).<sup>126</sup> The UCNPs@MS-Au<sub>25</sub> exhibited considerable PTT effect, by combining its intrinsic PDT effect to further enhance *in vivo* tumor inhibition under 808 nm laser.

Yang *et al.* fabricated metal-organic frameworks (MOFs) of  $Fe_3O_4/ZIF-8-Au_{25}$  (IZA) nanospheres.<sup>127</sup> The IZA nanospheres not only exhibited PTT effects upon NIR light irradiation to effectively kill tumor cells, but also proved useful in targeting and magnetic resonance imaging (MRI). The  $Au_{25}(Capt)_{18}$  in IZA

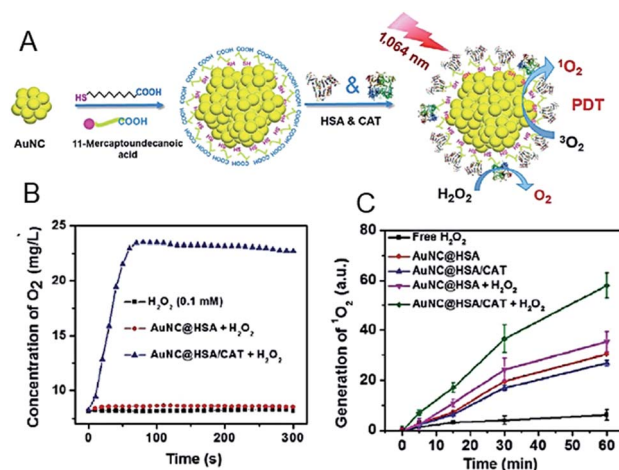


Fig. 20 (A) Synthesis and characterization of AuNC@HSA/CAT NPs. (B) Oxygen generation in  $H_2O_2$  solutions (100  $\mu$ M) incubated with AuNC@HSA or AuNC@HSA/CAT. (C) The generation of  $^1O_2$  determined by the increased SOSG fluorescence from AuNC@HSA or AuNC@HSA/CAT, with or without addition of  $H_2O_2$ . Panels (a)–(c) are reproduced with permission from ref. 98. Copyright 2018 Springer Nature.

nanospheres produced highly reactive  $^1O_2$  to cause PDT as well as PTT effects under NIR light irradiation. As a result, the IZA nanospheres exhibited synergistic therapeutic effect superior to any single therapy both *in vitro* and *in vivo* (Fig. 22A). Tumor-bearing mice treated only with PDT ( $Au_{25}(Capt)_{18}$  NCs under NIR) or PTT (IZ under NIR) displayed much less inhibition in tumor growth than those treated by the multimodal synergistic therapy with combined PDT, PTT, and MRI approaches (Fig. 22A).

Han *et al.* described a BSA-stabilized multifunctional theragnostic nanoplateform, gadolinium oxide–Au NCs–indocyanine green (ICG) hybrid ( $Gd_2O_3$ –BSA–AuNCs–ICG). The  $Gd_2O_3$ –AuNCs–ICG nanocomposites demonstrated excellent *in vivo* triple imaging capability for NIR fluorescence (NIRF), magnetic

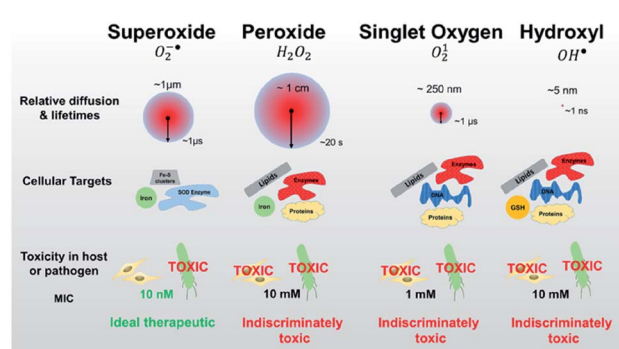


Fig. 21 Identifying pathogen vulnerability using redox perturbation with different ROS. Compared to singlet oxygen and hydroxyl radicals, superoxide and peroxide radicals have much longer diffusion lengths and half-lives in the cellular environment (red circles, not to scale). This figure is reproduced with permission from ref. 123. Copyright 2019 Springer Nature.



resonance, and computed topography, as well as efficacy in combined PDT and PTT (Fig. 22B).<sup>134</sup> Furthermore, Cui *et al.* constructed a nanocomposite of BSA-Au NCs-ICG to allow multimodal synergistic therapy, namely dual-modal NIRF/PA imaging, cancer treatment by synergistic action of PDT/PTT, and real-time therapeutic monitoring based on FRET.<sup>135</sup> Multimodal synergistic therapy using this nanocomposite resulted in 95% cancer cell death and complete tumor disappearance. Lv *et al.* produced a core/shell structured nanocomposite by conjugating  $\text{Au}_{25}(\text{SR})_{18}$  NC (a PDT/PTT agent), the pH/temperature-responsive polymer P(NIPAm-MAA), and the anti-cancer drug doxorubicin (DOX) onto the surface of mesoporous silica-coated core-shell up-conversion NPs (UCNPs) (Fig. 22C).<sup>129</sup> The controlled DOX release in the cancer cells was triggered by a high temperature from the PTT under NIR irradiation and low pH. The combined PDT, PTT, and pH/temperature-responsive chemo-T could significantly improve the therapeutic efficacy, as confirmed by both *in vitro* and *in vivo* assays. Moreover, the nanocomposite showed dual-modal imaging properties (computer tomography and up-conversion luminescence) when irradiated with 980 nm NIR light, demonstrating the potential for imaging-guided therapy.

In addition to their highly efficient  ${}^1\text{O}_2$  generation, the physiological properties of Au NCs in biological environments must be further evaluated in terms of the toxicity, renal clearance, and stability for *in vivo* PDT applications.<sup>136–147</sup> As for the renal clearance, NPs larger than 6 nm are eliminated from the blood stream by the reticuloendothelial system (RES; liver,

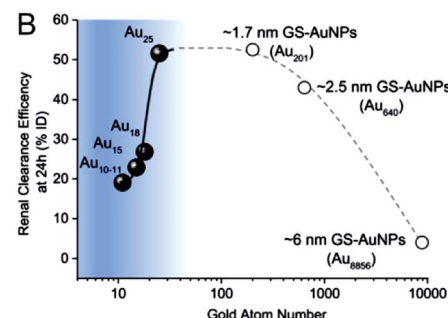
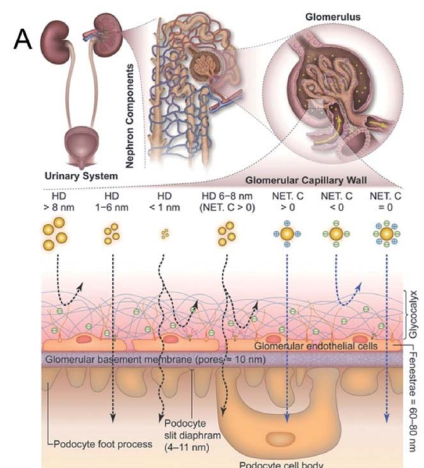


Fig. 23 (A) Transport of small NPs of different sizes and charges in the urinary system. A schematic shows three layered components of GCW, and the fate of small nanoparticles when reaching the capillary endothelium. (B) The relationship between Au atom numbers and renal clearance efficiency of SG-protected Au NPs (GS-Au NPs) at 24 h. The renal clearance efficiency dramatically decreased when the size of NPs  $< 1$  nm. Panel (a) is reproduced with permission from ref. 146. Copyright 2018 Wiley-VCH. Panel (b) is reproduced with permission from ref. 145. Copyright 2017 Springer Nature.

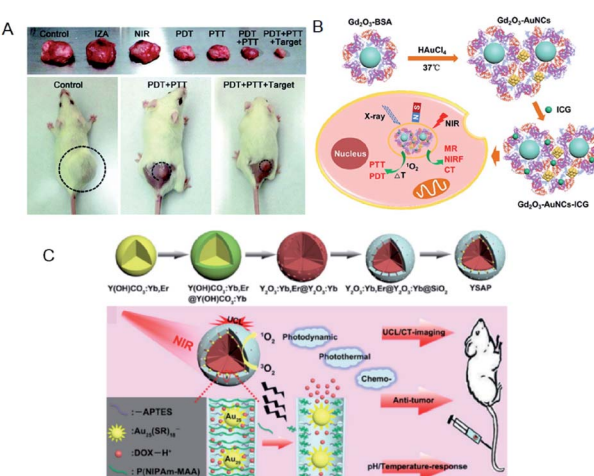


Fig. 22 (A) Photographs of tumor tissues excised from mice on the 14<sup>th</sup> day of treatment using normal saline, pure NIR laser, IZA:MOFs of  $\text{Fe}_3\text{O}_4/\text{ZIF}-8-\text{Au}_{25}$ , PDT (pure  $\text{Au}_{25}(\text{Capt})_{18}$  NCs under NIR), PTT (IZA under NIR), PDT + PTT, and PDT + PTT + magnetic stimulus. Bottom: photographs of representative tumor-bearing mice on the 14<sup>th</sup> day. (B) Schematic of  $\text{Gd}_2\text{O}_3$ -AuNCs-ICG nanohybrid as theragnostic agent for imaging-guided cancer therapy. (C) Schematic for the formation of  $\text{Y}_2\text{O}_3$ :Yb,Er@ $\text{Y}_2\text{O}_3$ :Yb@amSiO<sub>2</sub>-Au<sub>25</sub> P(NIPAm-MAA) and the imaging-guided synergistic multimodal anti-cancer therapy. Panel (a) is reproduced with permission from ref. 127. Copyright 2015 Royal Society of Chemistry. Panel (b) is reproduced with permission from ref. 134. Copyright 2017 American Chemical Society. Panel (c) is reproduced with permission from ref. 129. Copyright 2015 Elsevier Ltd.

spleen, *etc.*), while those smaller than 6 nm can be eliminated *via* the kidneys by passing through the glomerular capillary wall (GCW; *i.e.*, the kidney filtration) (Fig. 23A).<sup>136,146</sup> The longer circulation time of  $\text{Au}_{10,11}$  NCs in the blood compared to  $\text{Au}_{25}$  NCs allowed their accumulation in cancerous tissues through EPR (Fig. 23B).<sup>145</sup> The unique renal clearance behavior of the sub-nm Au NCs was explained by the filtration mechanism of GCW like-size separation utilizing size exclusive chromatography. Compared to the neutral NCs, it is more difficult for the negatively charged NCs to cross the GCW, since the GCW is negatively charged. Zwitterionic or non-ionic surface ligands (*e.g.*, SG or PEG) are desirable for the efficient urinary elimination of small NCs from the body.<sup>138,142,144,147</sup>

## 4. Conclusions and perspectives

In summary, we have reviewed the recent advances in the fields of photo/electrocatalysis and photosensitization using metal NCs, and their related green energy and medical applications. Owing to the unique properties of metal NCs, including their attractive photo-/electro-functional properties, as well as recent



developments in their atomically precise synthesis, these functionalized moieties show excellent potential for the abovementioned applications.

Considering the use of metal NCs in photo/electrocatalysis and photosensitization in green chemistry, we summarized several strategies to improve conversion efficiency and selectivity of the following materials: (i) electrocatalysts for water splitting and fuel cells, (ii) photocatalysts for water splitting, and (iii) solar cells. As described in this review, atomically precise control can contribute to the improvement of these materials. However, considering the practical applications, further developments are expected for simple and precise synthesis and isolation of metal NCs, as well as their loading. In addition, the following studies are envisaged for the improvement of these materials.

(1) Deeper understanding of the electronic structures of the loaded mono-metal and alloy NCs is essential for all of the applications. The electronic structures of the small NCs strongly depend on the number of the constituent atoms and the types of heteroatoms. Recent studies revealed the relationship between the electronic structures and these factors for the isolated NCs. However, the NCs loaded on the substrate seem to show different electronic structures as a result of the interaction between the NCs and the substrate, especially when the ligands are removed from the NC surface. It is expected that future studies would reveal the electronic structures of the loaded NCs for their application as active site on the substrate. In addition, the method for controlling the heteroatom position in the loaded alloy NCs is also expected to be developed in the future studies.

(2) For the improvement of photocatalysts, an effective method for separating  $e^- - h^+$  pairs should be established. The Fermi energy of the cocatalysts strongly affects the charge transfer of the excited electron. Therefore, the electronic structure of cocatalysts, which effectively facilitates the charge transfer from photocatalysts to cocatalysts must be designed. In addition, although most studies concentrate on the loading of cocatalysts only for the reduction reaction, the future studies should conduct the co-loading of the cocatalysts for both reduction and oxidation reactions. It is also important to deepen the understanding on the reaction intermediates, the mechanism, and the methods for suppression of the reverse reactions.

(3) Regarding the photosensitization application for solar cells, NCs, which are able to absorb the visible and infrared light to effectively use the sunlight, should be fabricated and utilized. The stability of NCs should also be improved for this application. In addition, improvements in the energy-conversion efficiency must be made by combining several systems.

Considering photosensitization of metal NCs for therapeutic applications, we summarized several strategies to improve the  $^1O_2$  generation efficiency and PDT activity of metal NCs: (i) atomically precise size control, (ii) NIR activation for deep-tissue treatments, (iii) AIE, (iv) RET, and (v) forming nanocomposites with other nanomaterials for multimodal synergistic therapy. Despite these efforts, further research into the following aspects is necessary:

(4) By adjusting  $n$  and  $m$ , the discrete electronic/geometrical structures of metals, and thereby their photosensitizing capability, can be controlled. Extensive studies on the syntheses of organo-soluble metal NCs with atomic precision have been described, while the synthesis of water-soluble metal NCs remains undeveloped. Therefore, further research into the synthesis of water-soluble metal NCs is required for therapeutic applications. Ligand exchange method using organo-soluble metal NCs may be useful for the synthesis of water-soluble metal NCs and alloy metal NCs would be valuable for the exploration of their photosensitizing capability.

(5) A photosensitizer is primarily required to possess the following properties:<sup>148</sup> (1) constant composition, (2) simplicity of synthesis, (3) lack of toxicity in the dark, (4) target specificity, (5) having a triplet state energy higher than 0.97 eV (the energy of single state oxygen,  $^1O_2$ ), (6) photostability, (7) high triplet state quantum yield, (8) fast clearance from the body, and (9) minimal self-aggregation. Metal NCs satisfy the above-mentioned requirements; however, their  $^1O_2$  generation efficiencies are lower than those of organic photosensitizers. The high triplet state quantum yield and inhibition of energy dissipation through non-radiative pathways would be the key factors to improve the  $^1O_2$  generation efficiency of the metal NCs. Since water-soluble thiolated metal NCs have multifunctionality such as imaging, drug delivery, and multiple sensitizing capability (photo-sensitizer, radiosensitizer, and sonosensitizer), it would be useful as a multipurpose ROS mediated nanomedicine<sup>84,85,149,150</sup>

(6) Regarding the *in vivo* PDT applications, the use of specific ligands for metal NCs increases the selectivity toward the target (e.g., cancerous tumors), an approach called “active targeting”. Targeting ligands on metal NCs are responsible for the selective interaction between the metal NCs and specific receptors on the surface of tumor cells, but not healthy cells, thus increasing the internalization of the NCs. Various types of surface modification of metal NCs, such as aptamer, specific peptides, glucose, DNA, and folic acid have been developed for efficient delivery of the metal NCs to the target (e.g., cancerous tumors) for *in vivo* applications.<sup>151–156</sup> Further studies involving active targeting of metal NCs would be important for *in vivo* PDT applications.

## Conflicts of interest

There are no conflicts to declare.

## Authorship contributions

*Photo/electrocatalysis of metal nanoclusters in green energy applications:* Tokuhisa Kawakami and Yuichi Negishi. *Photosensitization of metal nanoclusters for therapeutic applications:* Hideya Kawasaki. *Introduction and conclusion:* equal contribution by all authors.

## Notes and references

- 1 E. A. Dolgopolova, A. M. Rice, C. R. Martin and N. B. Shustova, *Chem. Soc. Rev.*, 2018, **47**, 4710–4728.



2 C. He, J. Cheng, X. Zhang, M. Douthwaite, S. Pattisson and Z. Hao, *Chem. Rev.*, 2019, **119**, 4471–4568.

3 X. Li, J. Yu, M. Jaroniec and X. Chen, *Chem. Rev.*, 2019, **119**, 3962–4179.

4 L. Liu and A. Corma, *Chem. Rev.*, 2018, **118**, 4981–5079.

5 O. Stroyuk, A. Raevskaya and N. Gaponik, *Chem. Soc. Rev.*, 2018, **47**, 5354–5422.

6 J.-D. Xiao and H.-L. Jiang, *Acc. Chem. Res.*, 2019, **52**, 356–366.

7 J. Zhao, W. Wu, J. Sun and S. Guo, *Chem. Soc. Rev.*, 2013, **42**, 5323–5351.

8 I. Chakraborty and T. Pradeep, *Chem. Rev.*, 2017, **117**, 8208–8271.

9 J. Yang, F. Wang, H. Yuan, L. Zhang, Y. Jiang, X. Zhang, C. Liu, L. Chai, H. Li and M. Stenzel, *Nanoscale*, 2019, **11**, 17967–17980.

10 S. Yougbare, T.-K. Chang, S.-H. Tan, J.-C. Kuo, P.-H. Hsu, C.-Y. Su and T.-R. Kuo, *Int. J. Mol. Sci.*, 2019, **20**, 2924.

11 H. Yu, B. Wao, W. Jiang, S. Yang and M. Zhu, *Coord. Chem. Rev.*, 2019, **378**, 595–617.

12 T. Higaki, Q. Li, M. Zhou, S. Zhao, Y. Li, S. Li and R. Jin, *Acc. Chem. Res.*, 2018, **51**, 2764–2773.

13 Q. Yao, T. Chen, X. Yuan and J. Xie, *Acc. Chem. Res.*, 2018, **51**, 1338–1348.

14 X. Kang and M. Zhu, *Chem. Soc. Rev.*, 2019, **48**, 2422–2457.

15 X. Jiang, B. Du, Y. Huang and J. Zheng, *Nano Today*, 2018, **21**, 106–125.

16 X. Dou, X. Chen, H. Zhu, Y. Liu, D. Chen, X. Yuan, Q. Yao and J. Xie, *Dalton Trans.*, 2019, **48**, 10385–10392.

17 Y. Su, T. Xue, Y. Liu, J. Qi, R. Jin and Z. Lin, *Nano Res.*, 2019, **12**, 1251–1265.

18 Y. Du, H. Sheng, D. Astruc and M. Zhu, *Chem. Rev.*, 2019, DOI: 10.1021/acs.chemrev.8b00726.

19 D. Wang, Z.-P. Liu and W.-M. Yang, *ACS Catal.*, 2018, **8**, 7270–7278.

20 J. Xing, H. B. Jiang, J. F. Chen, Y. H. Li, L. Wu, S. Yang, L. R. Zheng, H. F. Wang, P. Hu, H. J. Zhao and H. G. Yang, *J. Mater. Chem. A*, 2013, **1**, 15258–15264.

21 D. Wang, Z.-P. Liu and W.-M. Yang, *ACS Catal.*, 2017, **7**, 2744–2752.

22 Y.-G. Wang, Y. Yoon, V.-A. Glezakou, J. Li and R. Rousseau, *J. Am. Chem. Soc.*, 2013, **135**, 10673–10683.

23 H. Chen, P. Li, N. Umezawa, H. Abe, J. Ye, K. Shiraishi, A. Ohta and S. Miyazaki, *J. Phys. Chem. C*, 2016, **120**, 5549–5556.

24 N. Cheng, S. Stambula, D. Wang, M. N. Banis, J. Liu, A. Riese, B. Xiao, R. Li, T.-K. Sham, L.-M. Liu, G. A. Botton and X. Sun, *Nat. Commun.*, 2016, **7**, 13638.

25 S. Wang, X. Gao, X. Hang, X. Zhu, H. Han, W. Liao and W. Chen, *J. Am. Chem. Soc.*, 2016, **138**, 16236–16239.

26 X. Gao and W. Chen, *Chem. Commun.*, 2017, **53**, 9733–9736.

27 D. Eguchi, M. Sakamoto and T. Teranishi, *Chem. Sci.*, 2018, **9**, 261–265.

28 K. Kwak, W. Choi, Q. Tang, D.-e. Jiang and D. Lee, *J. Mater. Chem. A*, 2018, **6**, 19495–19501.

29 K. Kwak, W. Choi, Q. Tang, M. Kim, Y. Lee, D.-e. Jiang and D. Lee, *Nat. Commun.*, 2017, **8**, 14723.

30 K. Kwak and D. Lee, *Acc. Chem. Res.*, 2019, **52**, 12–22.

31 G. Hu, Q. Tang, D. Lee, Z. Wu and D.-e. Jiang, *Chem. Mater.*, 2017, **29**, 4840–4847.

32 W. Choi, G. Hu, K. Kwak, M. Kim, D.-e. Jiang, J.-P. Choi and D. Lee, *ACS Appl. Mater. Interfaces*, 2018, **10**, 44645–44653.

33 S. Zhao, R. Jin, Y. Song, H. Zhang, S. D. House, J. C. Yang and R. Jin, *Small*, 2017, **13**, 1701519.

34 Y. Du, J. Xiang, K. Ni, Y. Yun, G. Sun, X. Yuan, H. Sheng, Y. Zhu and M. Zhu, *Inorg. Chem. Front.*, 2018, **5**, 2948–2954.

35 P. Li, M. Wang, X. Duan, L. Zheng, X. Cheng, Y. Zhang, Y. Kuang, Y. Li, Q. Ma, Z. Feng, W. Liu and X. Sun, *Nat. Commun.*, 2019, **10**, 1711.

36 Y. Lee, J. Suntivich, K. J. May, E. E. Perry and Y. Shao-Horn, *J. Phys. Chem. Lett.*, 2012, **3**, 399–404.

37 G. Mattioli, P. Giannozzi, A. A. Bonapasta and L. Guidoni, *J. Am. Chem. Soc.*, 2013, **135**, 15353–15363.

38 R. Frydendal, E. A. Paoli, B. P. Knudsen, B. Wickman, P. Malacrida, I. E. L. Stephens and I. Chorkendorff, *ChemElectroChem*, 2014, **1**, 2075–2081.

39 K. S. Joya, L. Sinatra, L. G. AbdulHalim, C. P. Joshi, M. N. Hediili, O. M. Bakr and I. Hussain, *Nanoscale*, 2016, **8**, 9695–9703.

40 S. Zhao, R. Jin, H. Abroshan, C. Zeng, H. Zhang, S. D. House, E. Gottlieb, H. J. Kim, J. C. Yang and R. Jin, *J. Am. Chem. Soc.*, 2017, **139**, 1077–1080.

41 X. Zhao, P. Gao, Y. Yan, X. Li, Y. Xing, H. Li, Z. Peng, J. Yang and J. Zeng, *J. Mater. Chem. A*, 2017, **5**, 20202–20207.

42 P. C. Jennings, H. A. Aleksandrov, K. M. Neyman and R. L. Johnston, *Phys. Chem. Chem. Phys.*, 2014, **16**, 26539–26545.

43 A. Mahata, P. Bhauriyal, K. S. Rawat and B. Pathak, *ACS Energy Lett.*, 2016, **1**, 797–805.

44 K. A. Kacprzak, J. Akola and H. Häkkinen, *Phys. Chem. Chem. Phys.*, 2009, **11**, 6359–6364.

45 T. Imaoka, H. Kitazawa, W.-J. Chun and K. Yamamoto, *Angew. Chem., Int. Ed.*, 2015, **54**, 9810–9815.

46 K. Yamamoto, T. Imaoka, W.-J. Chun, O. Enoki, H. Katoh, M. Takenaga and A. Sonoi, *Nat. Chem.*, 2009, **1**, 397.

47 M. Nesselberger, M. Roefzaad, R. Fayçal Hamou, P. Ulrich Biedermann, F. F. Schweinberger, S. Kunz, K. Schloegl, G. K. H. Wiberg, S. Ashton, U. Heiz, K. J. J. Mayrhofer and M. Arenz, *Nat. Mater.*, 2013, **12**, 919–924.

48 T. Imaoka, H. Kitazawa, W.-J. Chun, S. Omura, K. Albrecht and K. Yamamoto, *J. Am. Chem. Soc.*, 2013, **135**, 13089–13095.

49 W. Chen and S. Chen, *Angew. Chem., Int. Ed.*, 2009, **48**, 4386–4389.

50 L. Wang, Z. Tang, W. Yan, H. Yang, Q. Wang and S. Chen, *ACS Appl. Mater. Interfaces*, 2016, **8**, 20635–20641.

51 L. Sumner, N. A. Sakthivel, H. Schrock, K. Artyushkova, A. Dass and S. Chakraborty, *J. Phys. Chem. C*, 2018, **122**, 24809–24817.

52 T. C. Jones, L. Sumner, G. Ramakrishna, M. b. Hatshan, A. Abuhagr, S. Chakraborty and A. Dass, *J. Phys. Chem. C*, 2018, **122**, 17726–17737.



53 Y. Lu, Y. Jiang, X. Gao and W. Chen, *Chem. Commun.*, 2014, **50**, 8464–8467.

54 D. R. Kauffman, D. Alfonso, C. Matranga, P. Ohodnicki, X. Deng, R. C. Siva, C. Zeng and R. Jin, *Chem. Sci.*, 2014, **5**, 3151–3157.

55 A. von Weber, E. T. Baxter, H. S. White and S. L. Anderson, *J. Phys. Chem. C*, 2015, **119**, 11160–11170.

56 H. Yin, H. Tang, D. Wang, Y. Gao and Z. Tang, *ACS Nano*, 2012, **6**, 8288–8297.

57 A. Fujishima and K. Honda, *Nature*, 1972, **238**, 37–38.

58 F. F. Schweinberger, M. J. Berr, M. Döblinger, C. Wolff, K. E. Sanwald, A. S. Crampton, C. J. Ridge, F. Jäckel, J. Feldmann, M. Tschurl and U. Heiz, *J. Am. Chem. Soc.*, 2013, **135**, 13262–13265.

59 M. J. Berr, F. F. Schweinberger, M. Döblinger, K. E. Sanwald, C. Wolff, J. Breimeier, A. S. Crampton, C. J. Ridge, M. Tschurl, U. Heiz, F. Jäckel and J. Feldmann, *Nano Lett.*, 2012, **12**, 5903–5906.

60 Y. Negishi, Y. Matsuura, R. Tomizawa, W. Kurashige, Y. Niihori, T. Takayama, A. Iwase and A. Kudo, *J. Phys. Chem. C*, 2015, **119**, 11224–11232.

61 W. Kurashige, R. Kumazawa, D. Ishii, R. Hayashi, Y. Niihori, S. Hossain, L. V. Nair, T. Takayama, A. Iwase, S. Yamazoe, T. Tsukuda, A. Kudo and Y. Negishi, *J. Phys. Chem. C*, 2018, **122**, 13669–13681.

62 Y. H. Li, J. Xing, Z. J. Chen, Z. Li, F. Tian, L. R. Zheng, H. F. Wang, P. Hu, H. J. Zhao and H. G. Yang, *Nat. Commun.*, 2013, **4**, 2500.

63 Y. H. Li, J. Xing, X. H. Yang and H. G. Yang, *Chem.-Eur. J.*, 2014, **20**, 12377–12380.

64 W. Kurashige, R. Hayashi, K. Wakamatsu, Y. Kataoka, S. Hossain, A. Iwase, A. Kudo, S. Yamazoe and Y. Negishi, *ACS Appl. Energy Mater.*, 2019, **2**, 4175–4187.

65 X. L. Du, X. L. Wang, Y. H. Li, Y. L. Wang, J. J. Zhao, L. J. Fang, L. R. Zheng, H. Tong and H. G. Yang, *Chem. Commun.*, 2017, **53**, 9402–9405.

66 K. Sridharan, E. Jang, J. H. Park, J.-H. Kim, J.-H. Lee and T. J. Park, *Chem.-Eur. J.*, 2015, **21**, 9126–9132.

67 Y.-S. Chen and P. V. Kamat, *J. Am. Chem. Soc.*, 2014, **136**, 6075–6082.

68 B. Weng, K.-Q. Lu, Z. Tang, H. M. Chen and Y.-J. Xu, *Nat. Commun.*, 2018, **9**, 1543.

69 N. Sakai and T. Tatsuma, *Adv. Mater.*, 2010, **22**, 3185–3188.

70 N. Sakai, S. Nakamura and T. Tatsuma, *Dalton Trans.*, 2013, **42**, 16162–16165.

71 N. Sakai, T. Ikeda, T. Teranishi and T. Tatsuma, *ChemPhysChem*, 2011, **12**, 2415–2418.

72 M. S. Kim, M. A. Abbas and J. H. Bang, *Bull. Korean Chem. Soc.*, 2016, **37**, 791–792.

73 V. Jeseentharani, N. Pugazhenthiran, A. Mathew, I. Chakraborty, A. Baksi, J. Ghosh, M. Jash, G. S. Anjusree, T. G. Deepak, A. S. Nair and T. Pradeep, *ChemistrySelect*, 2017, **2**, 1454–1463.

74 Y. Wang, X.-H. Liu, S. A. Kovalenko, Q.-Y. Chen and N. Pinna, *Chem.-Eur. J.*, 2019, **25**, 4814–4820.

75 Y.-S. Chen, H. Choi and P. V. Kamat, *J. Am. Chem. Soc.*, 2013, **135**, 8822–8825.

76 M. A. Abbas, T.-Y. Kim, S. U. Lee, Y. S. Kang and J. H. Bang, *J. Am. Chem. Soc.*, 2016, **138**, 390–401.

77 H. Choi, Y.-S. Chen, K. G. Stamplecoskie and P. V. Kamat, *J. Phys. Chem. Lett.*, 2015, **6**, 217–223.

78 D. C. Lim, B. Y. Seo, S. Nho, D. H. Kim, E. M. Hong, J. Y. Lee, S.-Y. Park, C.-L. Lee, Y. D. Kim and S. Cho, *Adv. Energy Mater.*, 2015, **5**, 1500393.

79 W. Fan, B. Yung, P. Huang and X. Chen, *Chem. Rev.*, 2017, **117**, 13566–13638.

80 J. Hu, Y. Tang, A. H. Elmenoufy, H. Xu, Z. Cheng and X. Yang, *Small*, 2015, **11**, 5860–5887.

81 M. Rizwan, T. Rasheed, A. Raza, M. Bilal, R. Yahya, M. Yar and H. M. N. Iqbal, *J. Drug Delivery Sci. Technol.*, 2019, **51**, 70–82.

82 J. Krajczewski, K. Rucińska, H. E. Townley and A. Kudelski, *Photodiagn. Photodyn. Ther.*, 2019, **26**, 162–178.

83 P. G. Calavia, G. Bruce, L. Pérez-García and D. A. Russell, *Photochem. Photobiol. Sci.*, 2018, **17**, 1534–1552.

84 S. Kwon, H. Ko, D. G. You, K. Kataoka and J. H. Park, *Acc. Chem. Res.*, 2019, **52**, 1771–1782.

85 B. Yang, Y. Chen and J. Shi, *Chem. Rev.*, 2019, **119**, 4881–4985.

86 M. Sakamoto, T. Tachikawa, M. Fujitsuka and T. Majima, *Langmuir*, 2009, **25**, 13888–13893.

87 T. Das, P. Ghosh, M. S. Shanavas, A. Maity, S. Mondal and P. Purkayastha, *Nanoscale*, 2012, **4**, 6018–6024.

88 H. Kawasaki, S. Kumar, G. Li, C. Zeng, D. R. Kauffman, J. Yoshimoto, Y. Iwasaki and R. Jin, *Chem. Mater.*, 2014, **26**, 2777–2788.

89 S. Miyata, H. Miyaji, H. Kawasaki, M. Yamamoto, E. Nishida, H. Takita, T. Akasaka, N. Ushijima, T. Iwanaga and T. Sugaya, *Int. J. Nanomed.*, 2017, **12**, 2703–2716.

90 C. Talavera and P. V. Kamat, *J. Chem. Sci.*, 2018, **130**, 1–7.

91 R. Ho-Wu, S. H. Yau and T. Goodson, *J. Phys. Chem. B*, 2017, **121**, 10073–10080.

92 C. Tominaga, H. Hasegawa, K. Yamashita, R. Arakawa and H. Kawasaki, *RSC Adv.*, 2016, **6**, 73600–73604.

93 Y. Yu, J. Geng, E. Y. X. Ong, V. Chellappan and Y. N. Tan, *Adv. Healthcare Mater.*, 2016, **5**, 2528–2535.

94 C. Tominaga, D. Hikosou, I. Osaka and H. Kawasaki, *Acta Phys.-Chim. Sin.*, 2018, **34**, 805–811.

95 Z. Liu, J. Wang, K. Qiu, X. Liao, T. W. Rees, L. Ji and H. Chao, *Chem. Commun.*, 2019, **55**, 6523–6526.

96 Q. Wang, Y. Dai, J. Xu, J. Cai, X. Niu, L. Zhang, R. Chen, Q. Shen, W. Huang and Q. Fan, *Adv. Funct. Mater.*, 2019, **29**, 1901480.

97 R. Vankayala, C.-L. Kuo, K. Nuthalapati, C.-S. Chiang and K. C. Hwang, *Adv. Funct. Mater.*, 2015, **25**, 5934–5945.

98 Q. Chen, J. Chen, Z. Yang, L. Zhang, Z. Dong and Z. Liu, *Nano Res.*, 2018, **11**, 5657–5669.

99 X. Chen, J. Song, X. Chen and H. Yang, *Chem. Soc. Rev.*, 2019, **48**, 3073–3101.

100 N. Goswami, Z. Luo, X. Yuan, D. T. Leonga and J. Xie, *Mater. Horiz.*, 2017, **4**, 817–831.

101 X.-D. Zhang, Z. Luo, J. Chen, S. Song, X. Yuan, X. Shen, H. Wang, Y. Sun, K. Gao, L. Zhang, S. Fan, D. T. Leong, M. Guo and J. Xie, *Sci. Rep.*, 2015, **5**, 8669.



102 T.-T. Jia, G. Yang, S.-J. Mo, Z.-Y. Wang, B.-J. Li, W. Ma, Y.-X. Guo, X. Chen, X. Zhao, J.-Q. Liu and S.-Q. Zang, *ACS Nano*, 2019, **13**, 8320–8328.

103 D. Luo, X. Wang, S. Zeng, G. Ramamurthy, C. Burda and J. P. Basilion, *Small*, 2019, **15**, 1900968.

104 F. Hu, S. Xu and B. Liu, *Adv. Mater.*, 2018, **30**, 1–29.

105 D. Hikosou, S. Saita, S. Miyata, H. Miyaji, T. Furuike, H. Tamura and H. Kawasaki, *J. Phys. Chem. C*, 2018, **122**, 12494–12501.

106 J. Xia, X. Wang, S. Zhu, L. Liu and L. Li, *ACS Appl. Mater. Interfaces*, 2019, **11**, 7369–7378.

107 H. Cao, Y. Qi, Y. Yang, L. Wang, J. Sun, Y. Li, J. Xia, H. Wang and J. Li, *Chem.-Asian J.*, 2018, **13**, 3540–3546.

108 X. Zhang, Y. Hu, X. Yang, Y. Tang, S. Han, A. Kang, H. Deng, Y. Chi, D. Zhu and Y. Lu, *Biosens. Bioelectron.*, 2019, **138**, 111314.

109 M. Yamamoto, K. Shitomi, S. Miyata, H. Miyaji, H. Aota and H. Kawasaki, *J. Colloid Interface Sci.*, 2018, **510**, 221–227.

110 K. G. Thomas and P. V. Kamat, *J. Am. Chem. Soc.*, 2000, **122**, 2655–2656.

111 K. G. Thomas and P. V. Kamat, *Acc. Chem. Res.*, 2003, **36**, 888–898.

112 F. Stellacci, C. A. Bauer, T. Meyer-Friedrichsen, W. Wenseleers, S. R. Marder and J. W. Perry, *J. Am. Chem. Soc.*, 2003, **125**, 328–329.

113 K. Pyo, N. H. Ly, S. M. Han, M. b. Hatshan, A. Abuhagr, G. Wiederrecht, S.-W. Joo, G. Ramakrishna and D. Lee, *J. Phys. Chem. Lett.*, 2018, **9**, 5303–5310.

114 V. Bonačić-Koutecký and R. Antoine, *Nanoscale*, 2019, **11**, 12436–12448.

115 A. Vangara, A. Pramanik, Y. Gao, K. Gates, S. Begum and P. C. Ray, *ACS Appl. Bio Mater.*, 2018, **1**, 298–309.

116 M. B. Smith and J. Michl, *Chem. Rev.*, 2010, **110**, 6891–6936.

117 T. Saegusa, H. Sakai, H. Nagashima, Y. Kobori, N. V. Tkachenko and T. Hasobe, *J. Am. Chem. Soc.*, 2019, **141**, 14720–14727.

118 L. Feng, F. He, Y. Dai, B. Liu, G. Yang, S. Gai, N. Niu, R. Lv, C. Li and P. Yag, *ACS Appl. Mater. Interfaces*, 2017, **9**, 12993–13008.

119 Y.-Y. Wang, Y.-C. Liu, H. Sun and D.-S. Guo, *Coord. Chem. Rev.*, 2019, **395**, 46–62.

120 X. Li, N. Kwon, T. Guo, Z. Liu and J. Yoon, *Angew. Chem., Int. Ed.*, 2018, **57**, 11522–11531.

121 A. R. Lippert, G. C. Van De Bittner and C. J. Chang, *Acc. Chem. Res.*, 2011, **44**, 793–804.

122 C.-P. Liu, T.-H. Wu, C.-Y. Liu, K.-C. Chen, Y.-X. Chen, G.-S. Chen and S.-Y. Lin, *Small*, 2017, **13**, 1700278.

123 M. Levy, P. P. Chowdhury and P. Nagpal, *J. Biol. Eng.*, 2019, **13**, 1–12.

124 D. Yang, A. Gulzar, G. Yang, S. Gai, F. He, Y. Dai, C. Zhong and P. Yang, *Small*, 2017, **13**, 1703007.

125 Y. Cheng, Y. Chang, Y. Feng, N. Liu, X. Sun, Y. Feng, X. Li and H. Zhang, *Small*, 2017, **13**, 1603935.

126 F. He, G. Yang, P. Yang, Y. Yu, R. Lv, C. Li, Y. Dai, S. Gai and J. Lin, *Adv. Funct. Mater.*, 2015, **25**, 3966–3976.

127 D. Yang, G. Yang, S. Gai, F. He, G. An, Y. Dai, R. Lv and P. Yang, *Nanoscale*, 2015, **7**, 19568–19578.

128 S. K. Katla, J. Zhang, E. Castro, R. A. Bernal and X. Li, *ACS Appl. Mater. Interfaces*, 2018, **10**, 75–82.

129 R. Lv, P. Yang, F. He, S. Gai, G. Yang, Y. Dai, Z. Hou and J. Lin, *Biomaterials*, 2015, **63**, 115–127.

130 F. Xia, W. Hou, C. Zhang, X. Zhi, J. Cheng, J. M. de la Fuente, J. Song and D. Cui, *Acta Biomater.*, 2018, **68**, 308–319.

131 X. Zan, Q. Li, Y. Pan, D. J. Morris, P. Zhang, P. Li, H. Yu and M. Zhu, *ACS Appl. Nano Mater.*, 2018, **1**, 6773–6781.

132 L. V. Nair, S. S. Nazeer, R. S. Jayasree and A. Ajayaghosh, *ACS Nano*, 2015, **9**, 5825–5832.

133 F. Gao, W. Zheng, L. Gao, P. Cai, R. Liu, Y. Wang, Q. Yuan, Y. Zhao and X. Gao, *Adv. Healthcare Mater.*, 2017, **6**, 1601453.

134 L. Han, J.-M. Xia, X. Hai, Y. Shu, X.-W. Chen and J.-H. Wang, *ACS Appl. Mater. Interfaces*, 2017, **9**, 6941–6949.

135 H. Cui, D. Hu, J. Zhang, G. Gao, Z. Chen, W. Li, P. Gong, Z. Sheng and L. Cai, *ACS Appl. Mater. Interfaces*, 2017, **9**, 25114–25127.

136 H. S. Choi, W. Liu, P. Misra, E. Tanaka, J. P. Zimmer, B. I. Ipe, M. G. Bawendi and J. V. Frangioni, *Nat. Biotechnol.*, 2007, **25**, 1165–1170.

137 A. Verma and F. Stellacci, *Small*, 2009, **6**, 12–21.

138 C. Zhou, M. Long, Y. Qin, X. Sun and J. Zheng, *Angew. Chem., Int. Ed.*, 2011, **50**, 3168–3172.

139 X. D. Zhang, D. Wu, X. Shen, P.-X. Liu, F.-Y. Fan and S.-J. Fan, *Biomaterials*, 2012, **33**, 4628–4638.

140 O. A. Wong, R. J. Hansen, T. W. Ni, C. L. Heinecke, W. S. Compel, D. L. Gustafson and C. J. Ackerson, *Nanoscale*, 2013, **5**, 10525–10533.

141 J. Liu, M. Yu, C. Zhou, S. Yang, X. Ning and J. Zheng, *J. Am. Chem. Soc.*, 2013, **135**, 4978–4981.

142 J. Liu, M. Yu, X. Ning, C. Zhou, S. Yang and J. Zheng, *Angew. Chem., Int. Ed.*, 2013, **52**, 12572–12576.

143 X.-D. Zhang, Z. Luo, J. Chen, H. Wang, S.-S. Song, X. Shen, W. Long, Y.-M. Sun, S. Fan, K. Zheng, D. T. Leong and J. Xie, *Small*, 2014, **11**, 1683–1690.

144 X. Ning, C. Peng, E. S. Li, J. Xu, R. D. Vinluan, M. Yu and J. Zheng, *APL Mater.*, 2017, **5**, 053406.

145 B. Du, X. Jiang, A. Das, Q. Zhou, M. Yu, R. Jin and J. Zheng, *Nat. Nanotechnol.*, 2017, **12**, 1096–1102.

146 J. Wang and G. Liu, *Angew. Chem., Int. Ed.*, 2018, **57**, 3008–3010.

147 L. Gong, Y. Chen, K. He and J. Liu, *ACS Nano*, 2019, **13**, 1893–1899.

148 R. Bakalova, H. Ohba, Z. Zhelev, M. Ishikawa and Y. Baba, *Nat. Biotechnol.*, 2004, **22**, 1360–1361.

149 Z. Lin, J. Song, X. Chen and H. Yang, *Angew. Chem., Int. Ed.*, 2019, DOI: 10.1002/ange.201906823.

150 K. Kawamura, D. Hikosou, A. Inui, K. Yamamoto, J. Yagi, S. Saita and H. Kawasaki, *J. Phys. Chem. C*, 2019, DOI: 10.1021/acs.jpcc.9b06849.

151 F. Ghahremani, D. Shahbazi-Gahrouei, A. Kefayat, H. Motaghi, M. A. Mehrgardi and S. H. Javanmard, *RSC Adv.*, 2018, **8**, 4249–4258.

152 B. N. P. Kumar, N. Puvvada, S. Rajput, S. Sarkar, M. K. Mahto, M. M. Yallapu, A. Pathak, L. Emdad,



S. K. Das, R. L. Reis, S. C. Kundu, P. B. Fisher and M. Mandal, *Mol. Pharm.*, 2018, **15**, 2698–2713.

153 F. Su, Q. Jia, Z. Li, M. Wang, L. He, D. Peng, Y. Song, Z. Zhang and S. Fang, *Microporous Mesoporous Mater.*, 2019, **275**, 152–162.

154 J. Lan, X. Wu, L. Luo, J. Liu, L. Yang and F. Wang, *Talanta*, 2019, **197**, 86–91.

155 A. Kefayat, F. Ghahremani, H. Motaghi and A. Amouheidari, *Nanomed. Nanotechnol. Biol. Med.*, 2019, **16**, 173–184.

156 G. S. Heo, Y. Zhao, D. Sultan, X. Zhang, L. Detering, H. P. Luehmann, X. Zhang, R. Li, A. Choksi, S. Sharp, S. Livingston, T. Primeau, D. E. Reichert, G. Sun, B. Razani, S. Li, K. N. Weilbaecher, F. Dehdashti, K. L. Wooley and Y. Liu, *ACS Appl. Mater. Interfaces*, 2019, **11**, 19669–19678.

